



## Article

# GNSS Real-Time Warning Technology for Expansive Soil Landslide—A Case in Ningming Demonstration Area

Zi Chen, Guanwen Huang \*, Wei Xie , Yongzhi Zhang and Le Wang

School of Geology Engineering and Geomatics, Chang'an University, Xi'an 710054, China; 2019026017@chd.edu.cn (Z.C.); chdxiewei@chd.edu.cn (W.X.); zhangyz@chd.edu.cn (Y.Z.); wangle18@chd.edu.cn (L.W.)

\* Correspondence: guanwen@chd.edu.cn; Tel.: +86-136-3680-1167

**Abstract:** Efficient monitoring and early warning are the preconditions of realizing expansive soil landslide hazard prevention and control. Previous early warning of expansive soil landslides was evaluated through soil sampling experiments to analyze the stability coefficient. However, the existing methods lack timeliness and ignore the inconsistent deformation characteristics of different parts of the landslide mass. There are still difficulties in the dynamic numerical early warning of landslides at multiple points. Considering that the degradation of expansive soil landslides' strength is directly reflected by surface displacement, for the Ningming expansive soil demonstration area and based on the GNSS shallow real-time displacement monitoring sequence, a landslide early-warning method based on the GNSS displacement rate combined with the GNSS displacement tangent angle model was proposed, and we thus designed early-warning thresholds for different warning levels. Combined with multi-source data such as soil moisture, soil pressure, and rainfall, the feasibility of accurate early warning of expansive soil landslides based on GNSS real-time surface displacement was verified. The proposed method does not require numerical calculation of internal stress and achieved two successful early warnings of landslides in the test area, which has a certain promotional value.

**Keywords:** expansive soil landslide; GNSS real-time monitoring; multi-source data; early-warning model; successful warning



**Citation:** Chen, Z.; Huang, G.; Xie, W.; Zhang, Y.; Wang, L. GNSS Real-Time Warning Technology for Expansive Soil Landslide—A Case in Ningming Demonstration Area. *Remote Sens.* **2023**, *15*, 2772. <https://doi.org/10.3390/rs15112772>

Academic Editor: José Fernández

Received: 22 April 2023

Revised: 22 May 2023

Accepted: 23 May 2023

Published: 26 May 2023



**Copyright:** © 2023 by the authors. Licensee MDPI, Basel, Switzerland. This article is an open access article distributed under the terms and conditions of the Creative Commons Attribution (CC BY) license (<https://creativecommons.org/licenses/by/4.0/>).

## 1. Introduction

Montmorillonite and other minerals are included in expansive clay, which is widely distributed in Shaanxi, Guangxi, the middle and lower reaches of the Yangtze River, and other regions in China. It is highly plastic and hydrophilic and is sensitive to environmental humidity. Expansive soil will expand when absorbing water, and it will shrink after losing water; therefore, it has an impact on the strength of building facilities or cutting slopes [1,2]. Many projects are impacted by expansive soil, such as the south–north water transfer project in central China, the expansive soil high fill airport in western China, and highway slopes in the Ningming Basin, Guangxi [3,4]. Therefore, expansive soil is known as “cancer soil in engineering”.

With the change of the water cycle inside the soil, the damage of expansive soil is repeated and continuous, which has a significant impact on shallow-foundation buildings [5], for instance, road surface uplift and the cracking of expansive soil subgrade, instable deformation of expansive soil cutting slopes, foundation movement or subsidence of houses in the expansive soil area, and other hazards [6]. If the warning of expansive soil landslide disaster is not issued in time, remedial and reinforcement measures can only be taken after the landslide failure, causing an increase in engineering costs. Moreover, the impact of expansive soil on engineering facilities cannot be avoided. The investigation of early-warning methods has become a key issue for expansive soil prevention and control engineering.

Sensors such as intelligent total stations, inclinometers, and earth pressure are mainly used by former researchers for expansive soil landslide monitoring data acquisition [7,8], but fewer studies focus on GNSS technology. GNSS positioning technology has the advantages of being low cost and real-time dynamic [9] and is widely used to investigate the motion of the earth surface and map tectonic strain patterns [10] and for early warning of geological landslides [11–16]. It can be applied to real-time monitoring and warning of expansive soil landslides. It is worth mentioning that ground-based and satellite-based InSAR technologies as an alternative to GNSS can provide higher spatial resolution and are also widely used to achieve long-term geological hazard monitoring [17–20]. In addition, in terms of numerical warning analysis, the research mainly focuses on the stability analysis of the landslide. Yang et al. [21] used the method of numerical simulation to conduct a finite element simulation of the water flow in the slope section, and the stability of the expansive soil slope was numerically evaluated. The spatial distribution and strength of filled cracks in slopes was considered [22], and a stability analysis method for expansive soil slopes with filled cracks was proposed. Chen et al. [23] applied the Swedish slice method to calculate the safety factor of an expansive soil slope in Zhenjiang, and in their research, the cracks in the slope were considered, and the safety factor was close to the actual result. The disadvantage of the above-mentioned method is that it needs soil experiments in advance in order to conduct computer simulation. It is difficult to carry out real-time dynamic early warning, and the deformation difference of different parts of the landslide is often not considered, which is inconsistent with the fragmentation of expansive soil landslides.

This paper focuses on the early warning of expansive soil landslides using GNSS technology. According to the GNSS monitoring equipment developed by the research team, a joint early-warning method based on the GNSS real-time displacement rate and GNSS tangent angle is proposed for the dynamic tracking and early warning of expansive soil landslides in the Ningming demonstration area. This method successfully warned the failure of local position in the slope twice. After the introduction, the overview of slope engineering and the construction of monitoring network in the demonstration area are first introduced. Then, the key monitoring parameters and principles of the demonstration area are introduced, respectively. Next, the real-time early-warning model, early-warning threshold, and early-warning system implementation process of expansive soil landslide based on single GNSS monitoring parameters are given. It can provide some reference advice for the prevention and control of expansive soil landslides in the Ningming area.

## 2. Introduction to the Test Area

### 2.1. Geological Information of the Test Area

The geographical location and satellite images of the test area are shown in Figure 1. The red star is the capital of Guangxi Province. It is in Ningming County in the southwest of Guangxi Province, China, and on the side of the Chong'ai Expressway at the border between China and Vietnam. The length and the maximum height difference in the slope are approximately 110 m and 12 m, with a slope ratio of 1:1.5. The initial development of fissures in the slope resulted in minor displacement due to the construction of the road and the excavation of the slope. To further limit the continuous deformation of the expansive soil slope, multi-layer geotextile bags were laid on the surface of the slope after excavation to reinforce the slope, and the surface of the geotextile bags was greened for reinforcement and protection.

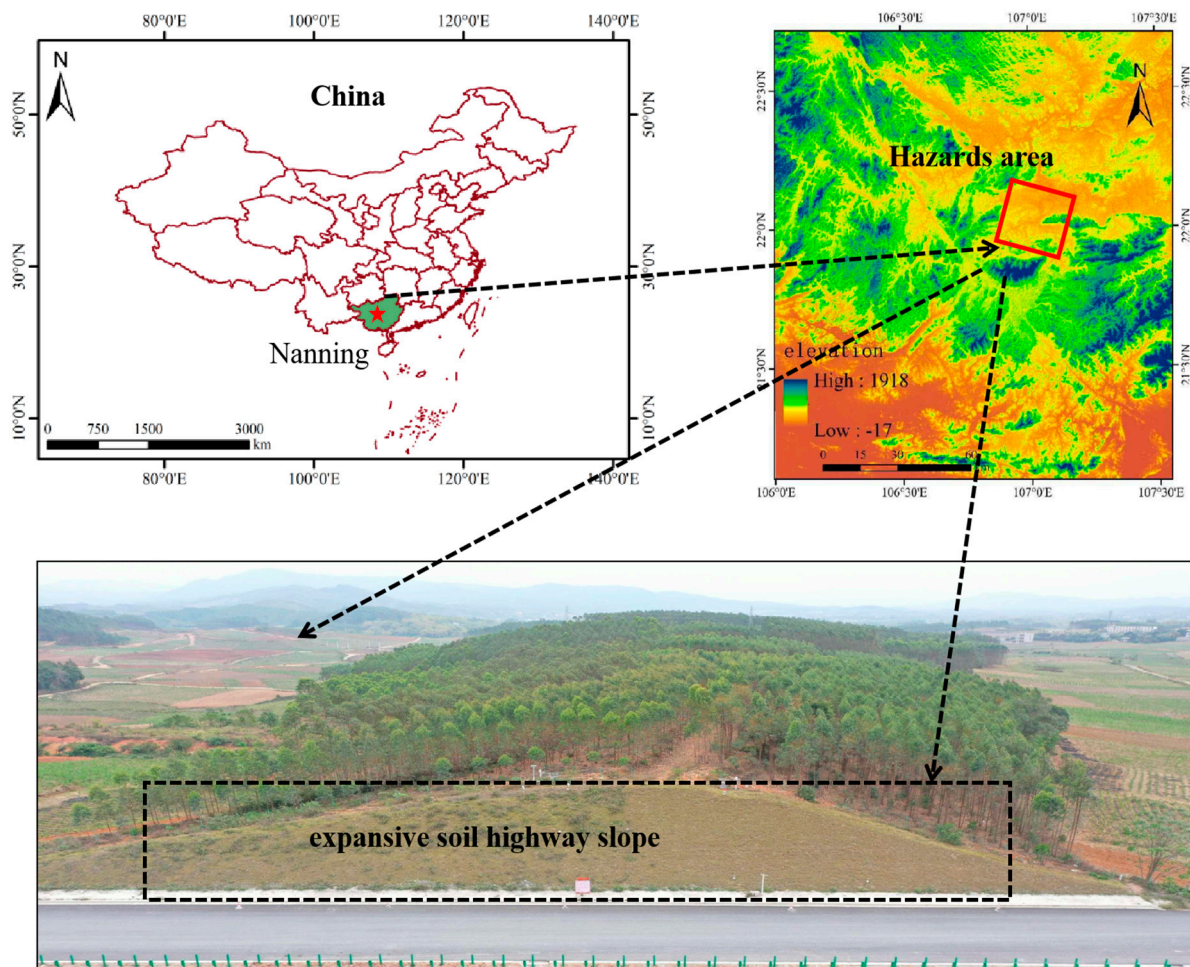


**Figure 1.** Location of Ningming expansive soil highway slope.

## 2.2. Construction of Monitoring Network in Landslide Demonstration Area

To establish a complete Ningming expansive soil landslide monitoring network, the four most important monitoring parameters, including GNSS surface displacement, supplemented by soil pressure, soil moisture content, and precipitation, were selected. The monitoring system includes three parts: (a) high-precision real-time monitoring sensors; (b) a stable network transmission system and power supply equipment; and (c) a reliable data processing cloud platform and early-warning-release system. The details of multi-source sensor layout are as follows:

The layout of GNSS monitoring points follows the principles of economy and rationality. The monitoring points were deployed at the slope shoulder–slope surface–slope toe, which is prone to deformation. Numbers 1~8 represent different GNSS monitoring points. According to the three-dimensional monitoring system composed of monitoring lines and monitoring points [24], the slope was divided into 1~5 sections and a~c layers; the average distance between sections is about 5.5 m; the height difference between them is about 4 m. GNSS monitoring units were deployed in areas with some cracks and relatively active deformation so that they can capture the displacement characteristics of the slope. As shown in Figure 2, eight GNSS monitoring units were deployed in total. On layer b, three sets of soil moisture meters (SF) were deployed from inside to outside with 20 cm. Regarding layer c, three sets of soil pressure cells were also deployed with 30 cm. Two sets of “shared power supply” integration stations and one rain gauge were added.

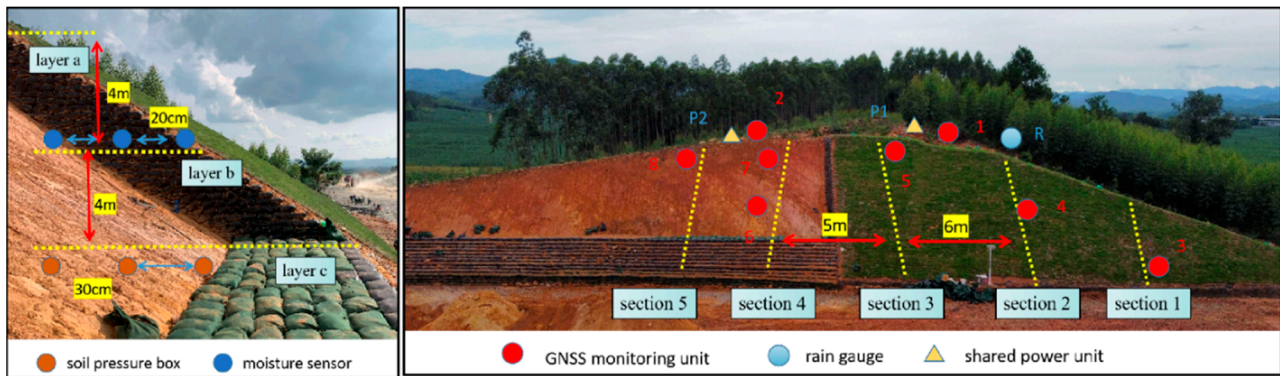


**Figure 2.** Landslide monitoring sensor deployment network.

### 3. Parameters Analysis of Expansive Soil Landslides Monitoring

#### 3.1. GNSS Real-Time Displacement Field Monitoring

The equipment structure and the displacement acquisition method are presented in Figure 3. The field displacement monitoring was based on self-developed GNSS monitoring equipment with a Ublox ZED-F9 P board. One monitoring reference station was established at the stable area, the monitoring stations are shown by red dots in Figure, and the average baseline length between the monitoring reference station and monitoring stations is 2.8 km. The data sampling rate was 1 s. The monitoring principle is as follows:

The multi-GNSS pseudo range and phase observations are received by monitoring equipment, then the RTK technology is used to obtain three-dimensional coordinates of monitoring stations. The measurement accuracy is better than 3 and 5 mm for horizontal and vertical directions, respectively. The difference between coordinates from RTK and initial reference coordinates are calculated, then transferring them to horizontal and vertical directions displacements. Thereafter, the displacements can be obtained. The detailed method to calculate displacement is as follows: First, the observation equation of GNSS real-time-kinematic (RTK) positioning is as follows:

$$\begin{aligned} \Delta\nabla P_i &= \Delta\nabla\rho + \Delta\nabla T + \mu_i\Delta\nabla I_i + \Delta\nabla e_i \\ \lambda_i\Delta\nabla\varphi_i &= \Delta\nabla\rho + \Delta\nabla T - \mu_i\Delta\nabla I_i + \lambda_i\Delta\nabla N_i + \Delta\nabla\varepsilon_i \end{aligned} \quad (1)$$

where  $\Delta\nabla$  is double-difference operator between satellites and stations;  $P$  and  $\varphi$  are pseudo range and phase observation, respectively;  $\mu$  is ionospheric delay coefficient;  $\rho$  is geometric distance between station and the satellite;  $T$  is tropospheric delay;  $I$  is ionospheric delay;  $e$  and  $\varepsilon$  are the pseudo range and phase observation noise, respectively.  $i$  is the observation frequency. Then, the coordinates transformation can be expressed as follows:

$$\begin{bmatrix} E_t \\ N_t \\ U_t \end{bmatrix} = \begin{bmatrix} -\sin B_M \cos L_M & -\sin B_M \sin L_M & \cos B_M \\ -\sin L_M & \cos L_M & 0 \\ \cos B_M \cos L_M & \cos B_M \sin L_M & \sin B_M \end{bmatrix} \begin{bmatrix} X_t - X_0 \\ Y_t - Y_0 \\ Z_t - Z_0 \end{bmatrix} \quad (2)$$

where  $E_t$ ,  $N_t$ , and  $U_t$  are the real-time displacement of the station in the east, north, and vertical directions at epoch  $t$ , respectively.  $B_M$ ,  $L_M$ , and  $H_M$  are the geodetic longitude, latitude, and elevation of the initial coordinates of the monitoring station.

#### 3.2. Soil Moisture Content

Soil moisture content is the ratio of water mass in the soil and soil particles' mass, and it is usually expressed as a percentage. A characteristic of expansive soil is sensitivity to water, as it can expand or shrink when absorbing or losing water, which is an important factor affecting the shear strength. Nine soil moisture meters were installed in the demonstration area; the measurement principle was to utilize electromagnetic pulses to measure the apparent dielectric constant of the soil, obtaining the real soil moisture content; its accuracy is  $\pm 3\%$ .

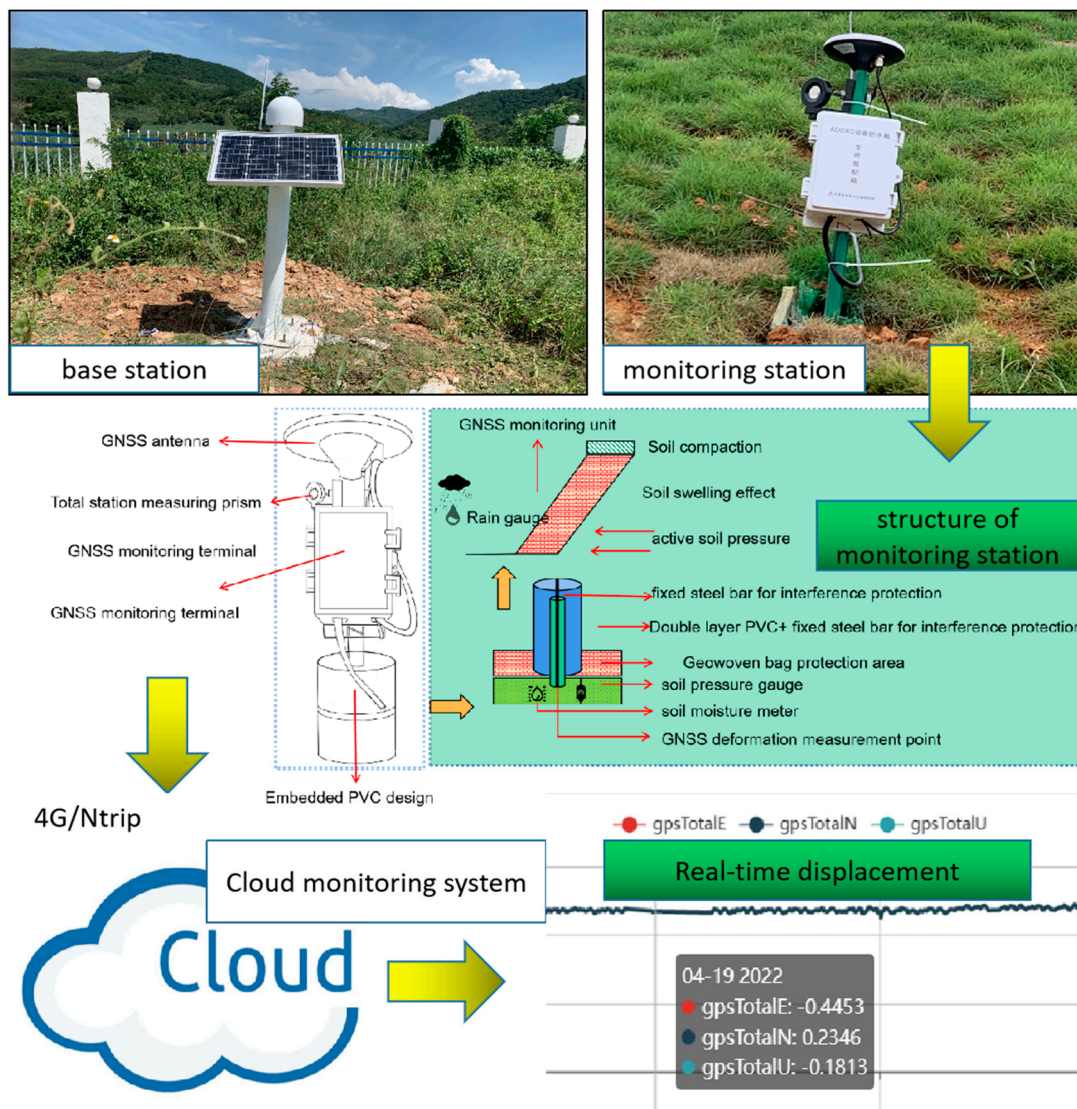


Figure 3. GNSS field monitoring device and principle.

### 3.3. Soil Pressure

Soil pressure is the force exerted by the soil on the retaining structure; its unit is Kpa. Thirty-nine flexible pressure boxes were deployed in the monitoring area to monitor the horizontal stress. For its measurement principle, the sensitive element of the flexible pressure boxes and force-bearing part of the sensor are fixed. The relationship between the natural frequency and impressed pressure of the rigid chord were applied to measure the stress. The nominal measurement accuracy of this sensor is  $\pm 0.5\%$  F.S.

### 3.4. Precipitation

Failure mode of ground displacement induced by rainfall could be deeply understood by precipitation monitoring. One funnel-type rainfall sensor was deployed in the demonstration area for data acquisition, and its measurement principle is that the rainwater enters the rain catcher, the tipping bucket will lose its balance and turn over when the accumulated water reaches a certain height; then, the precipitation result can be obtained by transforming the number of flips into a telecommunication signal in the rainfall process. Its nominal accuracy of measurement is  $\pm 0.2$  mm. Moreover, the signal will be transmitted to the monitoring system by the Nb-IoT technology. The details of the multi-source monitoring sensor installation for the slope in the demonstration area can be seen Figure 4.



**Figure 4.** Field diagram of multi-source monitoring sensors installed on slope. (a) Soil moisture meter. (b) Soil pressure box. (c) Rain gauge.

#### 4. Establishment of Expansive Soil Landslide Early-Warning Model

To effectively weaken the impact of the expansive soil landslide and engineering slope failure on engineering and residents, improving the efficiency of real-time monitoring and early warning is crucial. It is urgent to establish an effective early-warning model for instability, including early-warning methods, levels, and thresholds. Based on GNSS real-time shallow displacement data, a joint early-warning method was proposed by considering the GNSS displacement rate and improved tangent angle. Then, a three-level warning scheme (stable deformation, accelerated deformation, and instability) for expansive soil landslides was set up, which can provide a new reference for expansive soil landslides' early warning and engineering of slopes.

##### 4.1. Traditional Early-Warning Model Based on Environmental Parameter

###### 4.1.1. Critical Rainfall Warning

The critical rainfall warning is based on the historical data of rainfall-induced landslides, and the rainfall threshold model of landslides is established for the same or similar areas by analyzing the existing data [25]. For the determination of the critical rainfall threshold, a critical rainfall early-warning model was established according to the effective rainfall, which belongs to a regional or probabilistic warning method.

The rainfall intensity–duration threshold (ID) is the most widely applied critical rainfall model [26], and its comprehensive expression is as follows:

$$I = c + \alpha * D^{\beta} \quad (3)$$

where  $I$  denotes the hourly rainfall intensity;  $c$  denotes the initial rainfall;  $D$  denotes the rainfall time;  $\alpha$  and  $\beta$  are statistical parameters.

The relationship between rainfall intensity and duration was considered in this model: the critical rainfall intensity required for landslides gradually decreases with the increase of rainfall duration. Therefore, the early warning of landslides can be conducted by establishing a linear or nonlinear relationship between rainfall intensity and duration. If the historical rainfall–landslide data are insufficient, it is difficult to accurately conduct a meteorological early warning.

###### 4.1.2. Fissure Extent Warning

The engineering mechanical properties of expansive soils are influenced by some important factors such as the direction, width, depth and distribution density of fissures. The cracks' development can be quantified as an indicator, which is called fissure extent, to

perform the early warning of landslides. The fissure extent expression based on the crack area ratio was proposed [27], and it can be expressed as follows:

$$\delta_f = \frac{\sum_{i=1}^{n_f} A_i}{A} \quad (4)$$

where  $\delta_f$ ,  $n_f$ ,  $A_i$ , and  $A$  denote the fissure extent, total number of fissures, the area occupied by the  $i$ -th fissure, and the statistical sample area, respectively.

Although great progress has been made in modern fissure observation technology, in situ tests on slopes are required, so the calculation of fissure extent is still difficult, which makes it challenging to meet the real-time requirements of realistic hazard forewarning.

#### 4.2. GNSS Real-Time Early-Warning Model

The slope generally undergoes repeated stable deformation, accelerated deformation, and failure due to the multi-stage expansion and shrinkage characteristics of expansive soil landslides [28], and the shallow deformation may continue after one accelerated deformation or failure. The expansion and shrinkage deformation can be directly reflected by the surface displacement changes in different stages. The slope expansion deformation is particularly apparent during the seasons of heavy rainfall. Therefore, the GNSS real-time displacement monitoring technology was applied to capture shallow displacement changes, establishing an accurate early-warning model to reduce social losses caused by slope instability.

##### 4.2.1. Real-Time Early-Warning Model Based on GNSS Shallow Deformation

The stability of expansive soil landslide is a complex issue, and the shallow displacement rate is the most direct parameter to judge landslide motion state. However, this is only applicable to local scales due to the diversity of geological environment, expansion coefficient, and slope shape [29]. According to [30], for the gently expansive soil landslide area in the Ningming Basin, when it is not experiencing dramatic changes between drought and a wet environment, the landslide is generally in a stable state, and the displacement rate in this period falls into  $[V_a, V_b)$ .

When the slope is experiencing an obvious dry–wet variation, its current deformation state is easily changed. Then, the destruction process of the shallow surface accelerates, and the displacement rate increases significantly; its value falls into  $[V_b, V_c)$ . When the slope is impacted by several dry–wet cycles or short-term severe climate change, the fissures are fully developed, the sliding moment is increased because of the penetration force of the fissure water, and the landslide stability coefficient is significantly decreased. The slope will then enter the imminent instability stage. The displacement rate falls into  $[V_c, +\infty)$  in this period.

The early-warning criteria and thresholds for landslides in the Ningming demonstration area were preliminary given by combining several GNSS-measured displacement data and slope free expansion rate (57.5%) and the slope instability characteristics of gently expansive soil. The monitoring data of Chong'ai highway's expansive soil slope were used for validation.

When the slope is in the stable deformation stage, accelerated deformation stage, and imminent stability stage, the thresholds of  $V_a$ ,  $V_b$ , and  $V_c$  are 2 mm/d, 10 mm/d, and 30 mm/d, respectively. If the expansion coefficient is larger (the expansion effect is stronger), the alarm threshold can be appropriately reduced.

$$\begin{cases} V_a < V < V_b, & \text{in the stable deformation stage} \\ V_b \leq V < V_c, & \text{in the stage of accelerated deformation} \\ V_c \leq V, & \text{on the verge of instability} \end{cases} \quad (5)$$

Here,  $V_a$ ,  $V_b$ , and  $V_c$  represent the velocity thresholds when the slope enters the stages of stable deformation, accelerated deformation, and imminent instability, respectively.

The single displacement rate can affect the accuracy of early warning for expansive soil slopes, resulting in a false alert. When the slope is impacted by seasonally periodic effects or sudden climatic events, its displacement rate may suddenly rise, but it may not mean that the slope will collapse. Therefore, the GNSS displacement tangent angle was introduced to jointly identify the slope deformation state.

The cumulative displacement time series  $S - t$  was transferred by unifying the vertical and horizontal coordinate dimensions; then, the  $T - t$  curve was obtained. The GNSS tangent angle can be calculated according to the  $T - t$  curve.

The calculation formula is as follows:

$$\theta_i = \arctan \frac{T(i) - T(i - 1)}{t(i) - t(i - 1)} = \frac{\Delta T}{\Delta t} \tag{6}$$

where  $\theta_i$  denotes the improved tangent angle;  $T(i)$  and  $t(i)$  denote the vertical and horizontal coordinate value corresponding to the  $T - t$  curve after the coordinate transformation at the monitoring time  $i$ ; and  $\Delta T$  and  $\Delta t$  are the  $T(i)$  and  $t(i)$  variation within a monitoring period.

Compared to loess landslides, the creep characteristics of Ningming’s expansive soil are weaker, and its acceleration of deformation to instability is faster. Combining historical monitoring data and previous research theories on improving tangent angles, the pre-warning model is preliminarily defined as follows:

$$\left\{ \begin{array}{l} \theta_i < \theta_a, \text{ with fluctuation characteristics} \\ \theta_a \leq \theta_i < \theta_b, \text{ wave characteristics gradually disappear and change into monotonic rise} \\ \theta_b \leq \theta_i < 90^\circ, \text{ continues to increase and approaches } 90^\circ, \end{array} \right. \tag{7}$$

where  $\theta_a$  and  $\theta_b$  are the GNSS tangent angle thresholds when the slope enters the accelerated deformation and instability stages; they are  $80^\circ$  and  $85^\circ$ , respectively. The final early-warning model is shown in Table 1. When the GNSS displacement rate is less than 2 mm/d, the landslide displacement is subtle, and it has no risk of failure (blue). If the rate is between 2 mm/d and 10 mm/d, the GNSS tangent angle is less than  $80^\circ$ , and there is an oscillating characteristic, which brings the first warning level (yellow). The failure probability is very small, and only regular monitoring is required. If it is between 10 mm/d and 30 mm/d, the GNSS tangent angle is located between  $80^\circ$  and  $85^\circ$ , the deformation accelerates significantly, and the tangent angle increases monotonically, reaching the second warning level (orange). When it is larger than 30 mm/d, and the GNSS tangent angle exceeds  $85^\circ$ , the landslide mass is on the verge of instability and is at the alarm level (red).

**Table 1.** GNSS early-warning model of expansive soil landslide.

Warning Level	Criteria	Landslide State
No risk	$V < V_a$	Minor deformation stage
First level	$V_a \leq V < V_b$	Safe deformation stage
Second level	$V_b \leq V < V_c$	Accelerated deformation stage
Alarm level	$V_c \leq V$	On the verge of instability

#### 4.2.2. Implementation Process of GNSS Early-Warning System

The flowchart of the expansive soil landslide GNSS early-warning system is shown in Figure 5 and summarized as follows:

1. Real-time multi-GNSS monitoring data acquisition: Real-time stream observation data from monitoring stations and reference stations were collected; then, they were transmitted to the disaster monitoring cloud platform through 5G network/Ntrip protocol. This equipment was developed by our research group;
2. Data processing on cloud platform: This consists of observation outliers’ detection (preprocess layer), GNSS real-time relative positioning (monitoring layer), and smoothing filtering for the displacement time series (quality control layer);

3. Judgment of landslide instability: The GNSS displacement rate and tangent angle are the main warning parameters of the system, and capturing their variation is vital for early-warning analysis. If the displacement rate is beyond 30 mm/d, and the tangent angle is larger than  $85^\circ$  and without oscillation, it is considered that the landslide has entered the unstable state, and the warning message can be immediately issued. Furthermore, external multi-source data can be applied to support GNSS displacement determination, such as the correlation among multi-source data and whether the time–response relationship between external multi-source data and displacement exists or not;
4. If the degree of association among multi-source data is high, the slope mechanics model can be combined, and the instability mechanism of expansive soil slopes can be accurately interpreted, which can ensure the reliability of GNSS warning methods, especially for the following case: GNSS monitoring may experience unexpected interruptions due to communication issues or gross errors caused by complex observation environments. Multi-source data association changes or empirical warning methods can be used for timely compensation for these possible gross errors;

The specific early-warning model and early-warning level are shown in Table 1.

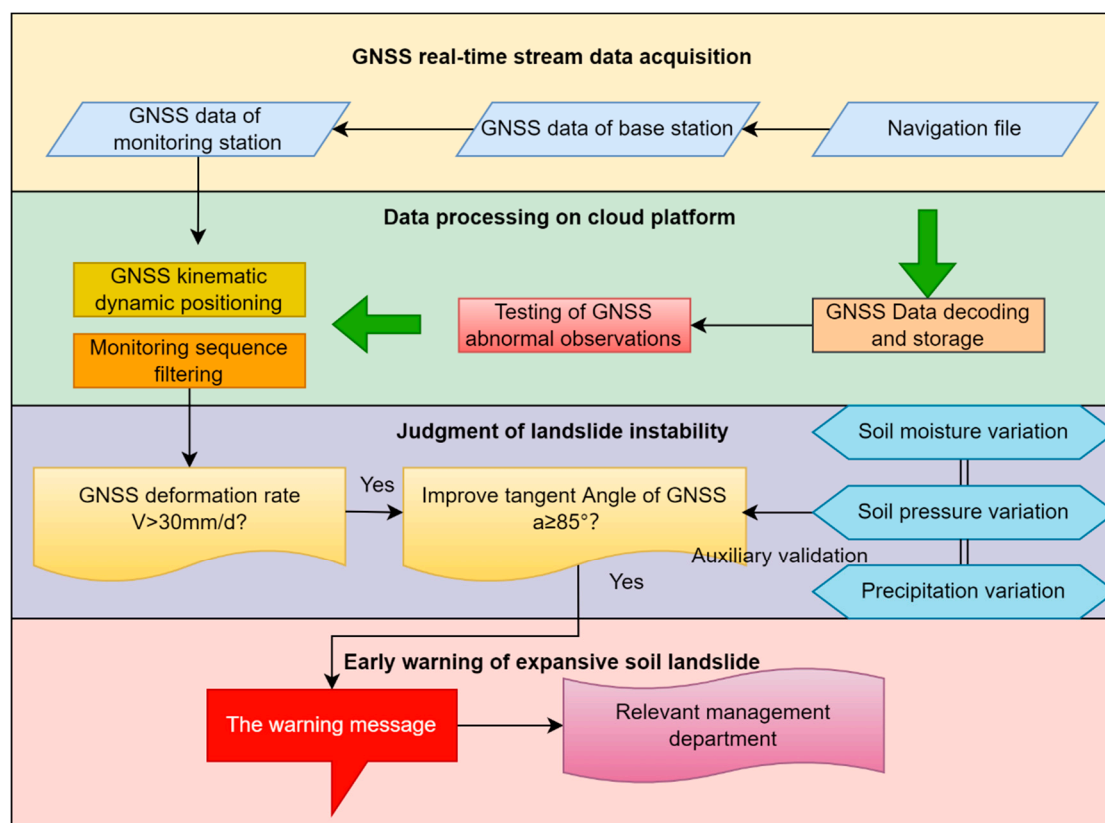


**Figure 5.** GNSS real-time early-warning process of expansive soil landslide.

## 5. Early-Warning Case Analysis of Test Area

For the expansive soil slope demonstration area in Ningming County, Chongzuo City, China, real-time single GNSS displacement monitoring data from 1 October 2021 to 11 October 2021 and 1 February 2022 to 22 February 2022 were collected. The early-warning parameter variation was tracked and analyzed by the real-time early-warning system. Two failures were successfully warned for this demonstration area.

### 5.1. GNSS Monitoring Results

The landslide displacement versus time data collected from GNSS monitoring equipment are shown in Figures 6 and 7 [31]. Two periods of significant deformation occurred at

NN06, NN07, and NN08 monitoring stations (the first and the second time was in October 2021 and February 2022, respectively), and there was no obvious deformation for other monitoring stations. Among them were some irregular displacements for NN06 from 7 February 2022 to 12 February 2022, which were caused by an interruption of data transmission.

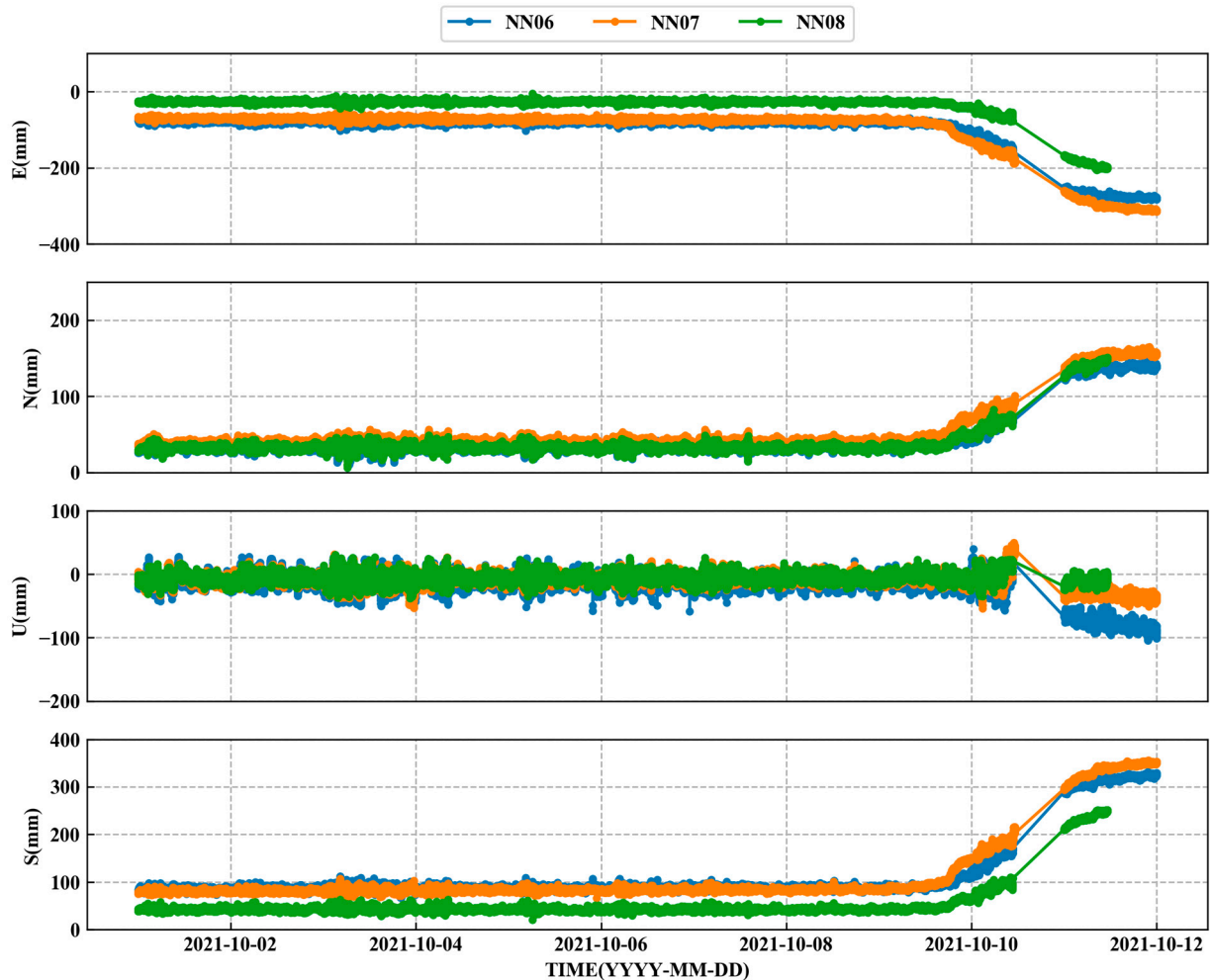


**Figure 6.** Raw displacement in different directions of each point in the first instability.

It can be seen from the Figures 6 and 7 that the two displacement curves had similar characteristics.

Taking the first instability as an example, the cumulative displacement of the three monitoring stations in E, N, U, and 3D directions remained stable before 9 October. The average rainfall intensity during this period is 0.602 mm/d, which is a dry period. At 00:00 on 9 October 2021, the cumulative displacements of the three monitoring stations in the 3D direction reached 89.02 mm, 83.53 mm, and 42.45 mm. However, at 13:10 on 9 October 2021, 6:02 on 9 October 2021, and 14:16 on 9 October 2021, the slope began to enter the accelerated deformation stage, with obvious increase trends appearing for the east and north directions. At about 17:00 on 11 October 2021, the displacement of the monitoring station reached its maximum value, and the three-dimensional displacements were 323.41 mm, 348.06 mm, and 246.79 mm, respectively. After checking the rainfall data, it was known that the displacement increment was larger than 200 mm within 3 days, according to the rainy trend during this period. It can be inferred that the expansive soil slope became unstable in this area in which the horizontal displacement was significant, while the vertical displacement was not, and the sudden change of displacement was significantly related to the precipitation. The three-dimensional displacement curve has

obvious mutation characteristics from its original stability to its final failure. Therefore, it is feasible to use real-time GNSS displacement for early warning.

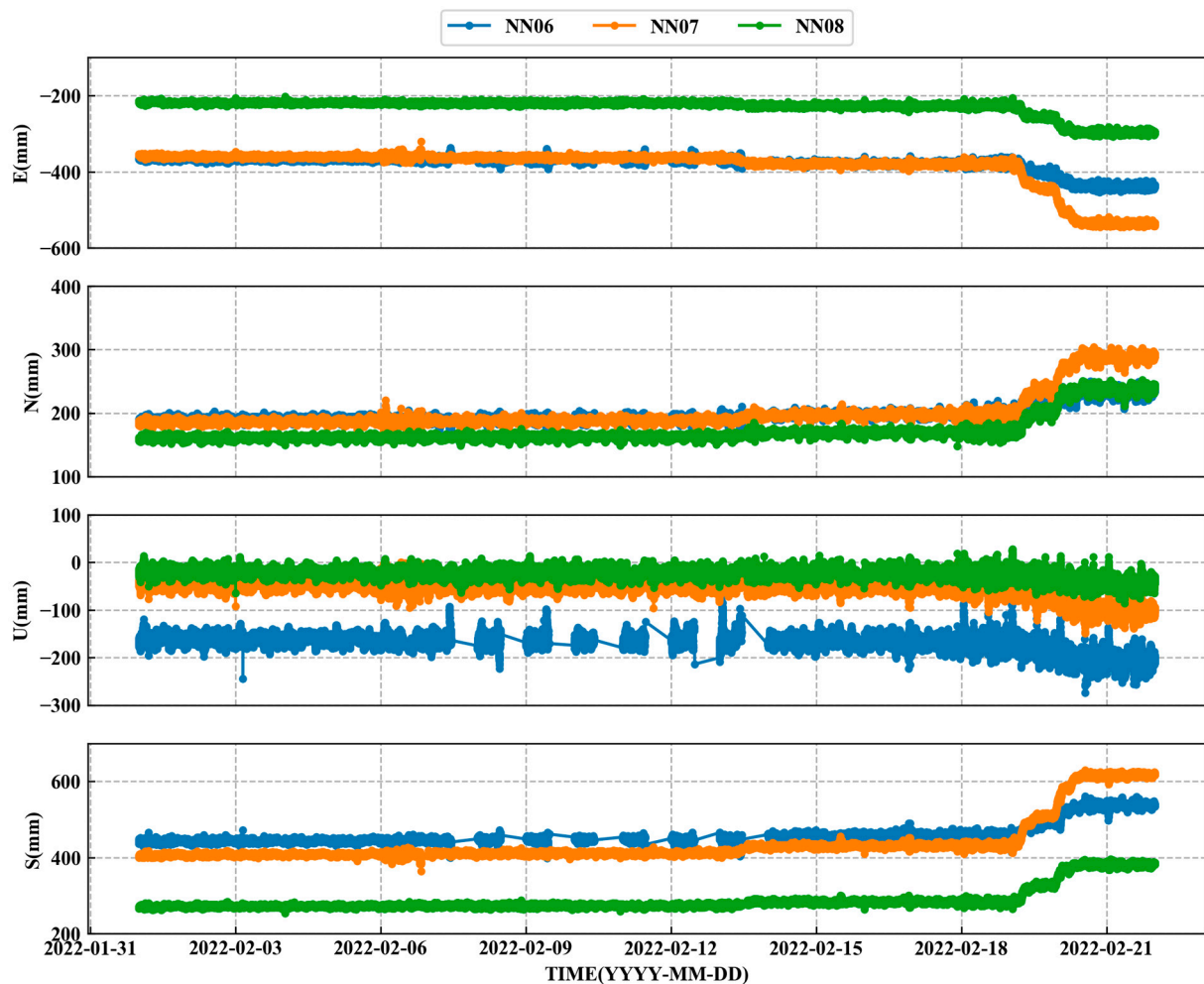


**Figure 7.** Raw displacement of each point in different directions in the second instability.

## 5.2. GNSS Real-Time Warning Results

### 5.2.1. The First Instability Early-Warning Case

The first slope failure occurred on 11 October 2021; it was in the middle and upper layers of the slope, i.e., between the fourth and fifth sections (in Figure 2). The landslide area was about 104 square meters. Since 1 October 2021, eight GNSS displacement monitoring sensors were deployed, and the complete 1 Hz real-time GNSS displacement results were estimated using the monitoring and early-warning system.

After calculating the monitoring coordinate time series, the early-warning processing can be conducted by the cloud platform to track the variation of key parameters including real-time displacement of the ground surface, displacement rate, and GNSS tangent angle; these can be calculated and published per day/hour/second.

The different stability stages can be obtained according to judgement method of the early-warning model (Table 1). The displacement rate in each direction (daily solution) obtained using the early-warning system based on the accumulative displacement is shown in Figure 8. For NN06, NN07, and NN08 monitoring stations, the displacement rate in the horizontal direction is larger than that in the vertical one. The main reason is the dominant lateral expansion force. The lateral deformations also lead to the increase of the distribution of further cracks after the failure, which is due to the superficial failure feature of common gently expansive soil slopes for the Ningming Basin [32]. The displacement rate of the monitoring stations in the first seven days was stable (0.42 mm/d, 0.02 mm/d,

and 0.07 mm/d for NN06, NN07, and NN08 stations, respectively). On 8 October 2021, the slope acceleration trends were sensitively found by the early-warning system, thus beginning the preparation of the early warning. Nevertheless, it is unreliable to judge the slope stability using only a single rate or tangent angle indicator, which is proven in the next warning case.

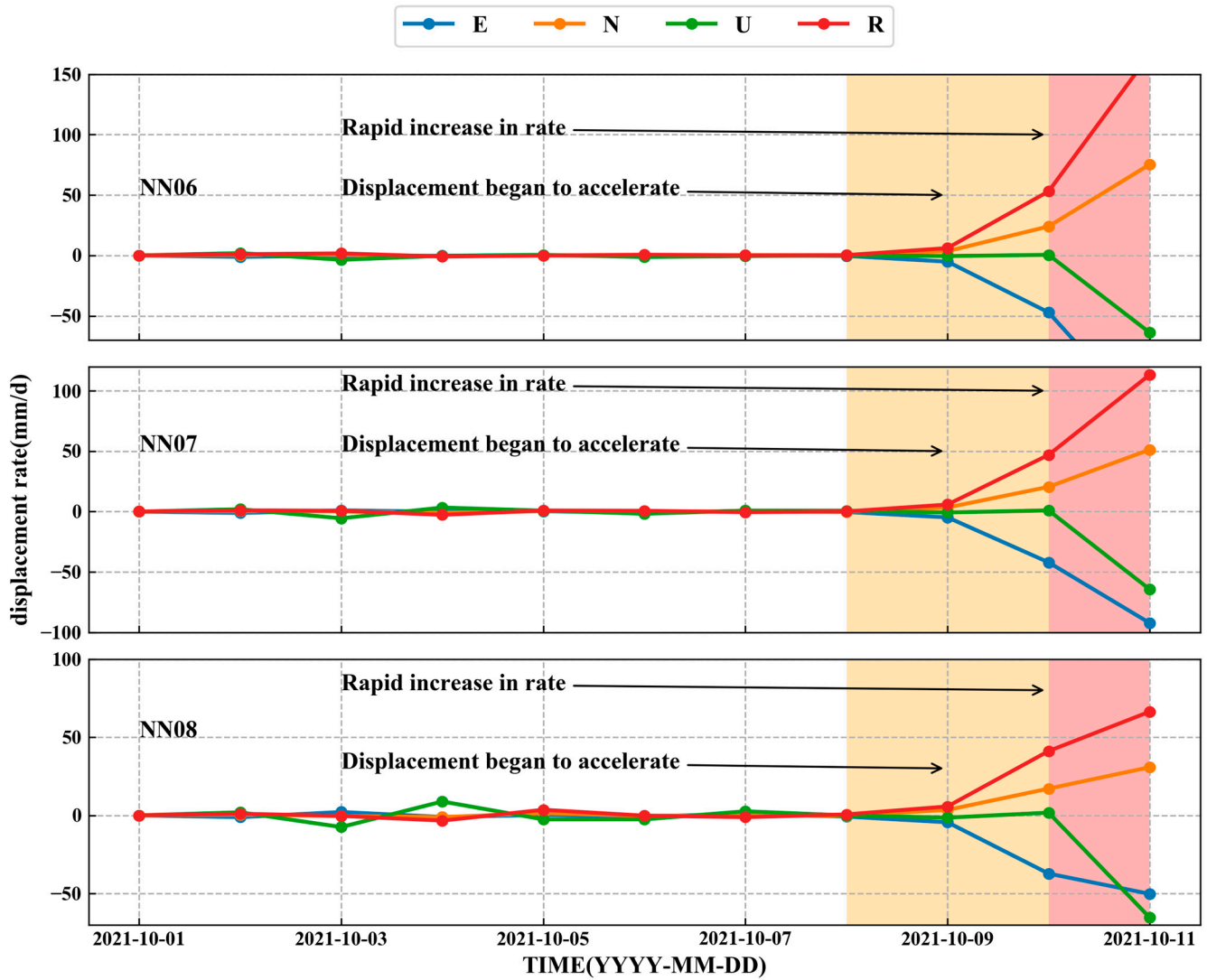


**Figure 8.** Displacement rate curve of monitoring points (2021/10. E, east; N, north; U, elevation; R, 3D direction).

GNSS displacement information can be calculated and tracked by real-time warning system. The real-time GNSS surface displacement, displacement rate, and improved tangent angle curves of unstable areas are shown in Figure 9a–c.

The obvious deformation instability area is near the fourth and fifth section. Before 8 October 2021, the real-time displacement rate of the NN06 station was less than 10 mm/d, and the tangent angle was continuously oscillating below 80°. The stable deformation stage was judged by the early-warning system, and the probability of failure was very low; thus, only regular monitoring was required.

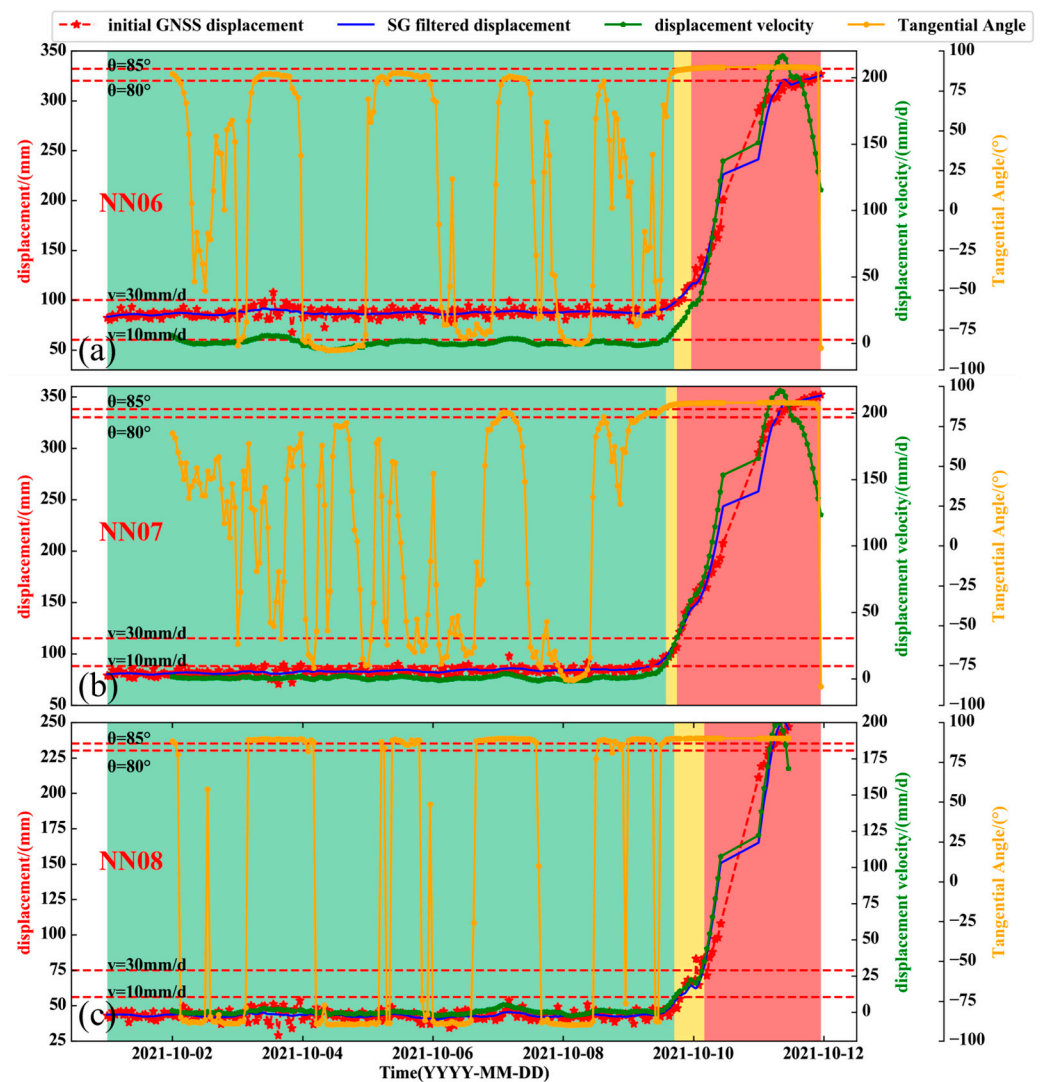


**Figure 9.** First instability real-time warning information: (a) NN06; (b) NN07; (c) NN08.

At 0:02 on 10 October 2021, 18:05 on 9 October 2021, and 3:36 on 10 October 2021 for NN06, NN07, and NN08, both the rate and tangent angle began to exceed the default alarm threshold, and the oscillation characteristics of tangent angle disappeared. A red alarm was sent out by the warning system. The landslide process was preliminarily divided into different stages (green, yellow, and red represent stable deformation stage, accelerated deformation stage, and near instability stage, respectively) according to different levels of alarm conditions, which are marked in Figure 9. The warning was issued by the system, which was about 47 min earlier than the real failure on average. The detailed early-warning time and warning time in advance can be seen in Table 2. After landslide, a field investigation was conducted, as is shown in Figure 10. Compared with before the landslide, four obvious fissure areas (1–4) were found in the yellow frame, and all of them were distributed on the slope shoulder with an average length of 9 cm. The specific failure position of the slope is shown in Figure 11. The red frame is the instability boundary, and the blue dotted line represents sections 4 and 5. By conducting the investigation, it was found that the drainage trough was choked on the rear boundary of the slope body. A great amount of rainwater infiltrated into this area; obvious shallow damage near this area occurred, and it was repaired in time after the shallow slide.

**Table 2.** Information about the first successful early warning.

Deformation Point	First Level	Second Level	Alarm Level	Displacement Rate (mm/d)	Tangent Angle (°)	Warning Time (min)
NN06	2021/10/3-04:02	2021/10/9-18:32	2021/10/09-23:52	30.02	89.17°	52
NN07	2021/10/4-14:12	2021/10/9-13:58	2021/10/9-17:50	31.21	88.98°	55
NN08	2021/10/6-22:51	2021/10/9-16:50	2021/10/10-03:32	30.58	89.96°	34

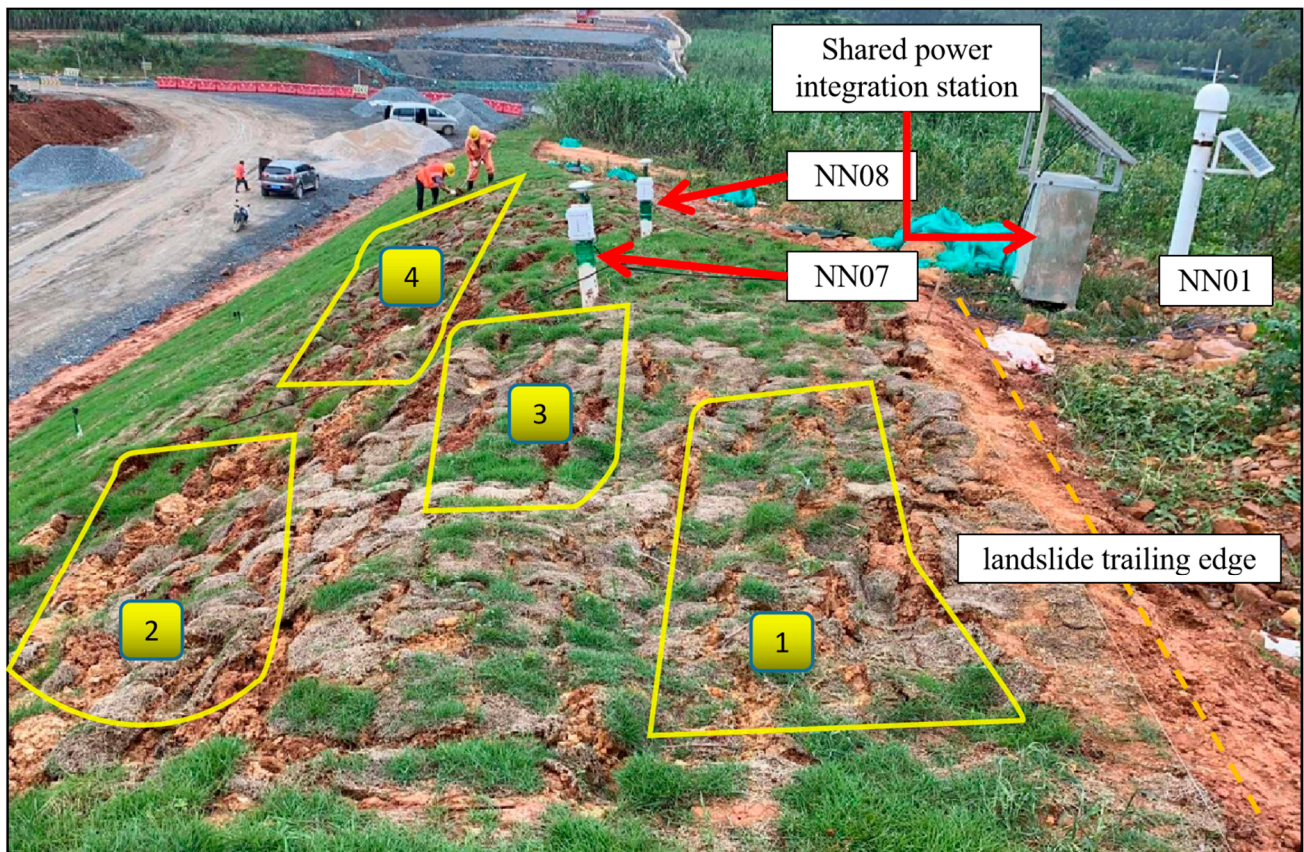


**Figure 10.** Shallow deformation on slope shoulder and rear edge.

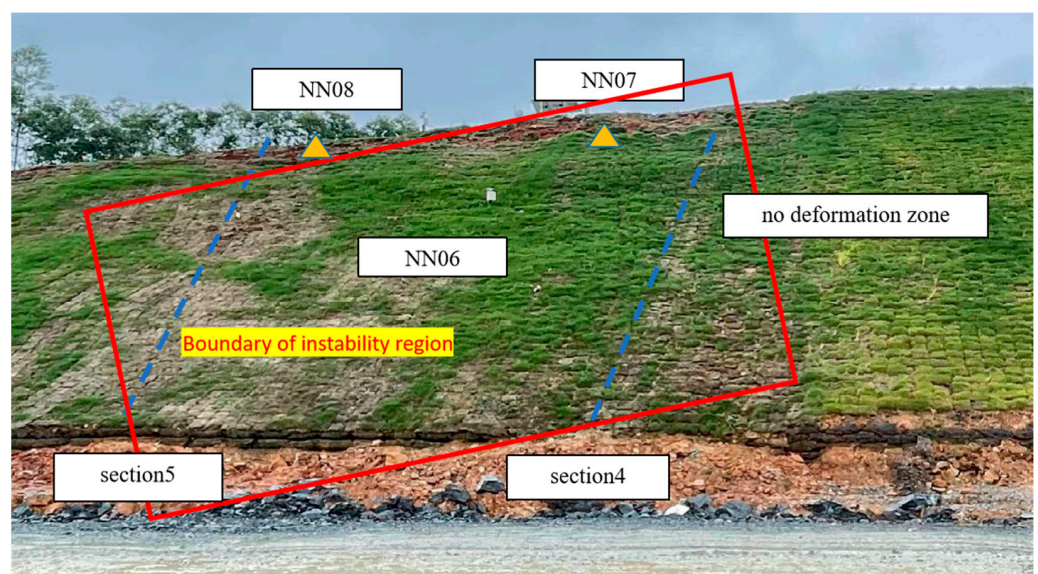


**Figure 11.** Instability area in the first failure.

### 5.2.2. The Second Case of Instability Warning

Another slope instability occurred in February 2022. Similarly to the first landslide, it was caused by short-term heavy rainfall, and the failure form was shallow, local instability; it is shown in Figure 12 that the displacement of the slope was stable during the first 17 days, deformation was captured by the early-warning system on 18 February 2022, and after deformation acceleration, the early-warning system prepared to track and analyze the alarm parameters.

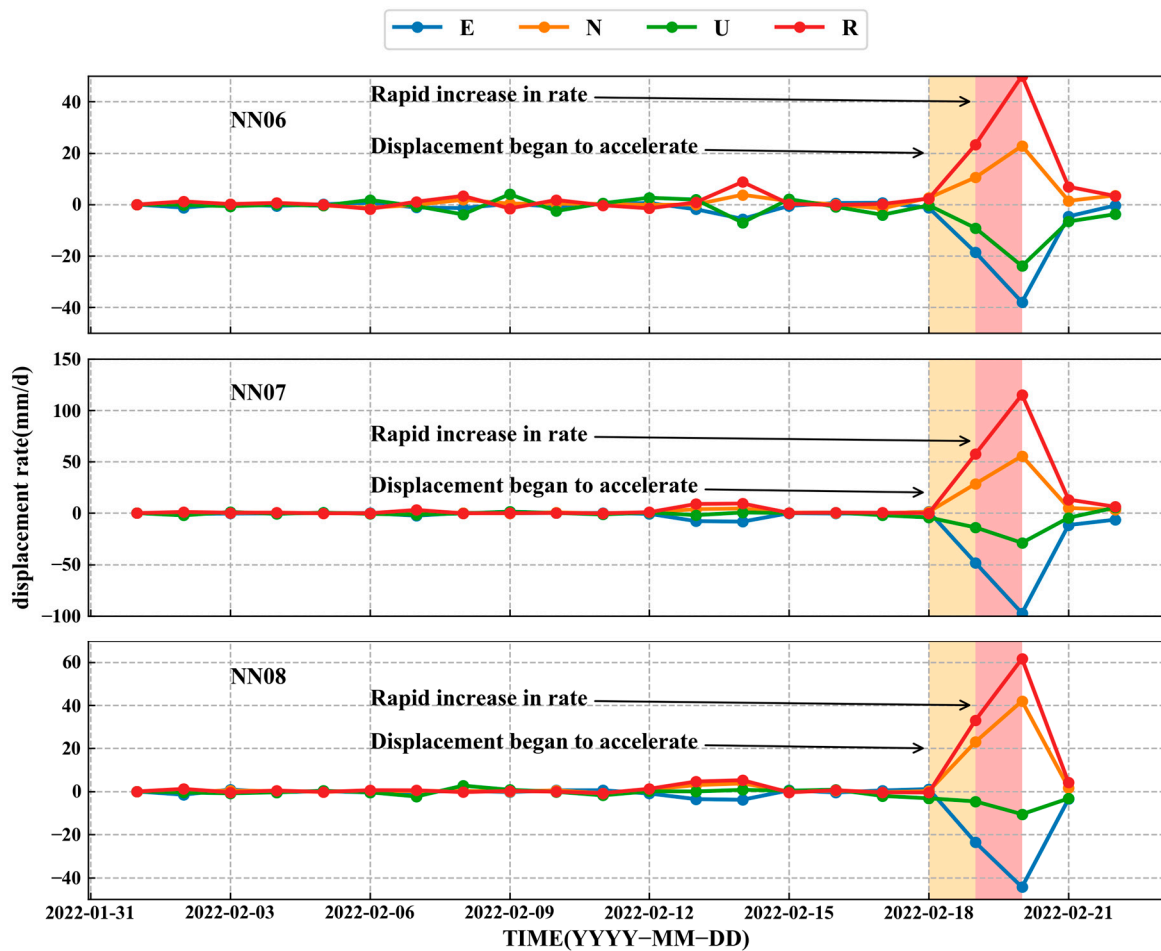


Figure 12. Displacement rate curve of monitoring points (2022/02. E, east; N, north; U, elevation; R, three-dimensional direction).

Figure 13a–c show that the real-time curves of GNSS surface displacement, displacement rate, and improved tangent angle were processed by the early-warning system during the second instability period. As of 17 February 2022, there was no distinct deformation at the three stations, while for the NN06 station, the rate and tangent angle were 30.35 mm/d and 88.05° at 13:50 on 19 February 2022, respectively. In terms of the NN07 station, the rate and tangent angle were 29.13 mm/d and 88.98° at 4:24 on 19 February 2022, respectively. For the NN08 station, the rate and tangent angle were 30.86 mm/d and 89.51° at 8:42 on 19 February 2022, respectively. The warning principle was required, and the researchers sent an alarm message after a brief analysis. The detailed warning level division, alert time, and advance alarm time are shown in Table 3.

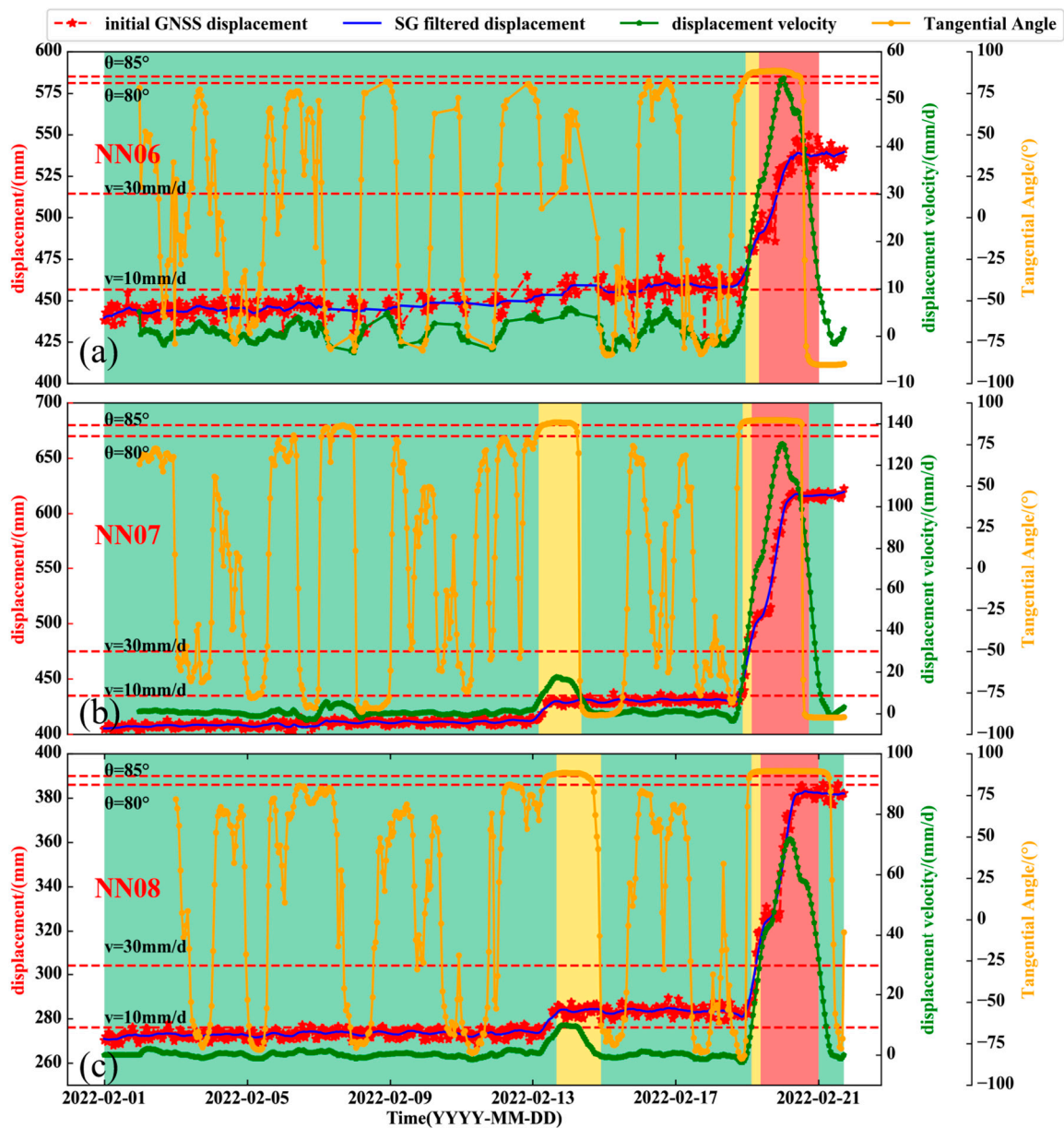


Figure 13. The second instability real-time warning information: (a) NN06; (b) NN07; (c) NN08.

Table 3. Information related to the second successful early warning.

Deformation Point	First Level	Second Level	Alarm Level	Displacement Rate (mm/d)	Tangent Angle (°)	Warning Time (min)
NN06	2022/2/3-13:45	2022/2/19-05:21	2022/2/19-14:00	31.56	88.13°	45
NN07	2022/2/7-04:10	2022/2/13-13:00	2022/2/19-04:30	30.58	89.22°	75
NN08	2022/2/6-22:51	2022/2/13-16:08	2022/2/19-08:52	31.35	89.54°	50

The NN06 station experienced three deformation stages (stable–acceleration–failure), while NN07 and NN08 experienced five stages, namely “stable–acceleration–stable–acceleration–failure”, which is a representative failure mode of rain-induced expansive soil landslides [33]. For the first accelerated deformation stage, the tangent angle exceeded 85° from 9:00 on 13 February to 9:00 on 14 February, but the average displacement rates were 17.2 mm/d and 10.2 mm/d, respectively. The numerical value increased significantly, whereas it did

exceeded the threshold; there was indeed stability near the two monitoring stations during this period, and this proves that it is inappropriate to use a single indicator to judge the state of the landslide. Hence, it is improper to estimate a landslide's state with only one parameter.

As shown in Figure 14, The red frame shows the visible cracks near the station after failure, compared with the first slope failure, the cracks on the surface were denser and more developed, and some parts were severely damaged this time.



**Figure 14.** The rupture near GNSS monitoring station after the second failure.

For example, the soil mass near the slope surface of NN08 was obviously collapsed (red frame in the figure), the slope displacement gradually recovered on the 21st, and the value of the early-warning parameters dropped significantly and accordingly.

## 6. Discussion

### 6.1. Correlation between GNSS Parameters and Multi-Source Data

#### 6.1.1. Results of Multi-Source Monitoring Data

##### 1. Soil moisture content

The soil moisture content versus time for the first landslide at NN06, NN07, and NN08 is shown in Figure 15. The soil moisture content sensors SF1 and SF2 are near NN06, NN07, and NN08 stations, respectively. The soil moisture content slowly declined at the two sensors, SF1 and SF2, in the early stage of monitoring, which can be attributed to the fact that the main dry and wet effect of the slope was dominated by evaporation. After entering the rainfall period on 9 October 2021, the soil moisture content at SF1 and SF2 was increased about 8% and 7% within 3 days, respectively; it was increased simultaneously with the rainfall. The lag period between soil moisture content and the rainfall was very short, and the nearby GNSS monitoring displacements simultaneously experienced obvious uplifts.

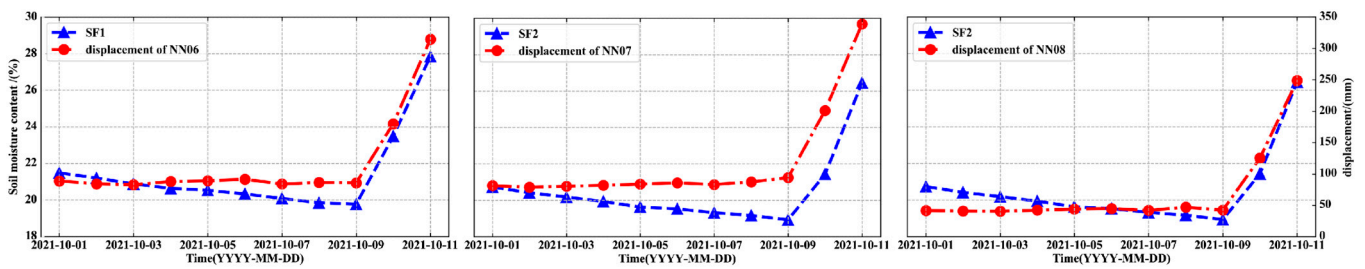


Figure 15. Monitoring curves of soil moisture content at different location.

## 2. Soil pressure

The soil pressure value can reflect the expansive force variation in expansive soil [34]; the monitoring results are shown in Figure 16.

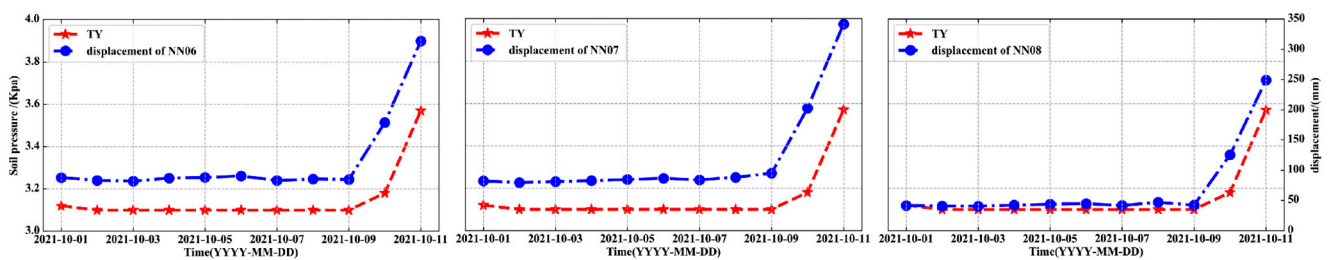


Figure 16. Numerical curves of earth pressure at different positions.

When the slope experiences meteorological events such as heavy rainfall [35], the soil inner pressure also accordingly changes. In the no-rain period, the displacement of the slope was slight, the slope was in the process of drought and shrinkage, and the additional thrust could not be received for the sensors embedded in five sections of the slope. Therefore, the soil pressure was nearly constant. Under rainfall conditions, water was absorbed by the soil behind the sensors, producing obvious force perpendicular to the soil pressure box; thus, the horizontal soil pressure increased accordingly. During the accelerated deformation of the slope, the soil pressure value also had a corresponding sudden change.

## 3. Precipitation

The precipitation monitoring results during the two instability periods in this area are shown in Figure 17. The first and second landslides occurred in a dry period before 8 October 2021 and 17 February 2022; the cumulative rainfall and soil pressure remained stable, and there were periodic fluctuations of the ground temperature. From October 8 to 11 October 2021, the cumulative precipitation continued to rise in the rainy period, with an average rain intensity of 30.2 mm/d. The rainfall was also intensive from 17 February to 20 February 2022, and these two periods were continuous heavy rainfall periods. During these two periods, the soil pressure and surface temperature increased and decreased, respectively. The precipitation was the direct cause of the significant change in GNSS displacement of the expansive soil slope.

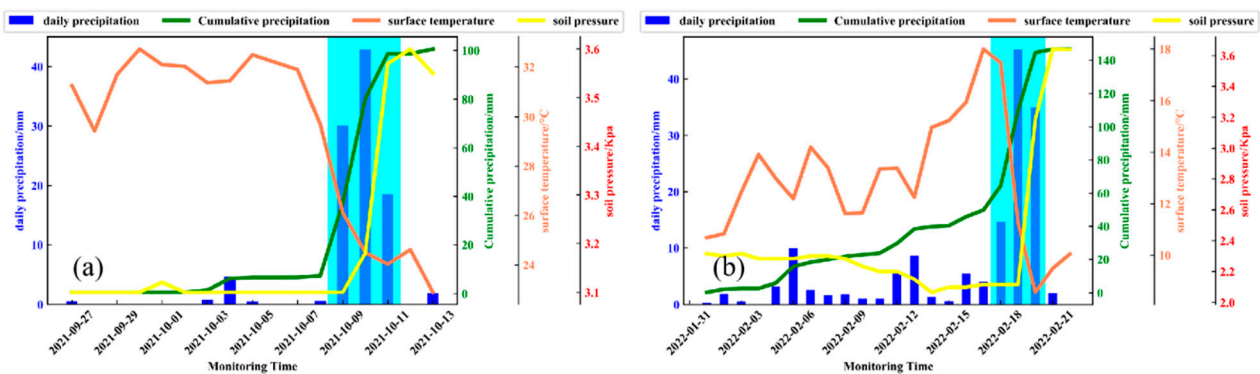


Figure 17. Monitoring results of precipitation. (a)The first failure. (b)The second failure.

### 6.1.2. Response Relationship between Multi-Source Data and GNSS Displacement

Taking the second failure as an example, the multi-source monitoring parameters are shown in Figure 18. Before 17 February 2022, the average daily rainfall was 2.93 mm, which was in a dry period, and the displacement rate remained stable. A heavy rainfall event was occurred on 17 February to 20 February 2022, with an average daily rainfall of 31.62 mm. During the rainy period, the GNSS displacement rate increased significantly at three stations. During this stage, the GNSS displacement was accelerated, and the tangent angle showed a monotonous increase. On 22 February 2022, the slope returned to stability, and soil moisture content and soil pressure showed a sudden change at same time. The monitored values of the soil moisture content near NN06 and NN07 increased by 6.88% and 3.68%, respectively. It is worth noting that small rainfall events around 13 February 2022 also caused a small increase in the ground deformation rates at NN07 and NN08, but it did not exceed the warning threshold. The nearby soil moisture content phased increased, and the GNSS tangential angle also shortly exceeded  $85^\circ$ , showing a characteristic of highly consistent change. Soil pressure, moisture content, rainfall, displacement rate, and GNSS tangential angle showed an obvious time response, and the correlation coefficient was 0.9 (strong correlation). There was a lag effect between GNSS displacement rate and rainfall, and the lag time was about 1 d.

The cause for the two slope failures was continuous heavy rainfall events. The development of multi-layer cracks during the dry period, which provided a good opportunity for the increase in soil moisture in rainy season [36], resulted in a sharp increase in the moisture content in this slope, causing continuous deformation of the soil and sudden changes in internal stress. The stability gradually decreased until the shallow layer became unstable, leading to eventual failure. The sliding direction was consistent with the changing direction of the GNSS stations (northwest, approximately perpendicular to the slope trend), indicating that the second failure was a continuation of the first failure, which validates the characteristic of repeated instability of expansive soil landslides. The synchronous response relationship of source monitoring data proved that it is feasible to use only GNSS surface displacement for early warning.

### 6.1.3. The Relationship between Displacement Rate and Rainfall Occurrence

Figures 19 and 20 show the lag correlation curves of displacement rate and rainfall during the first and second instability, respectively: (a), (b), and (c) are the horizontal direction; (d), (e), and (f) are the vertical direction; each column represents NN06, NN07, and NN08; the horizontal axis represents the offset time (d); the negative number represents the lag time; and the positive number represents the advance time. It can be seen from the figure that in the first failure, when the lag time of the horizontal and vertical displacement rate and rainfall is 1 d and 2 d respectively, the correlation reaches the extreme value. In the second failure, when the lag time of the horizontal and vertical displacement rate and rainfall is 0 d and 1 d, respectively, the correlation reaches the extreme value. The extreme values of lag correlation and lag time of each point are shown in Table 3. Therefore, the

response time of soil and rainfall is within 3 d, and the horizontal displacement rate is 1 d earlier than the vertical direction for Ningming’s expansive soil demonstration area. This is due to the fact that the lateral expansive force is dominant in expansive soil deformation, and horizontal-direction deformation is more sensitive than that in the vertical direction.

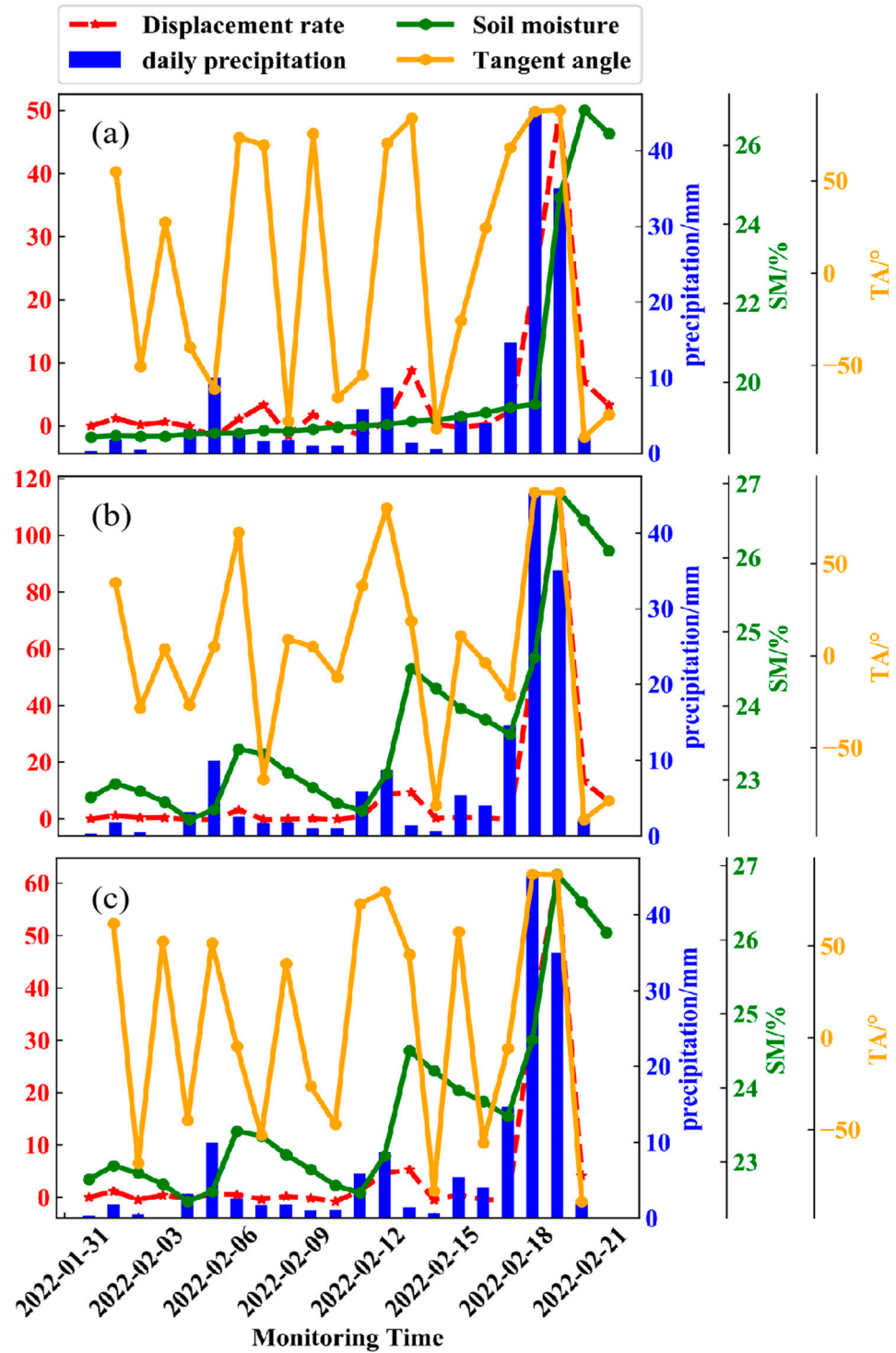
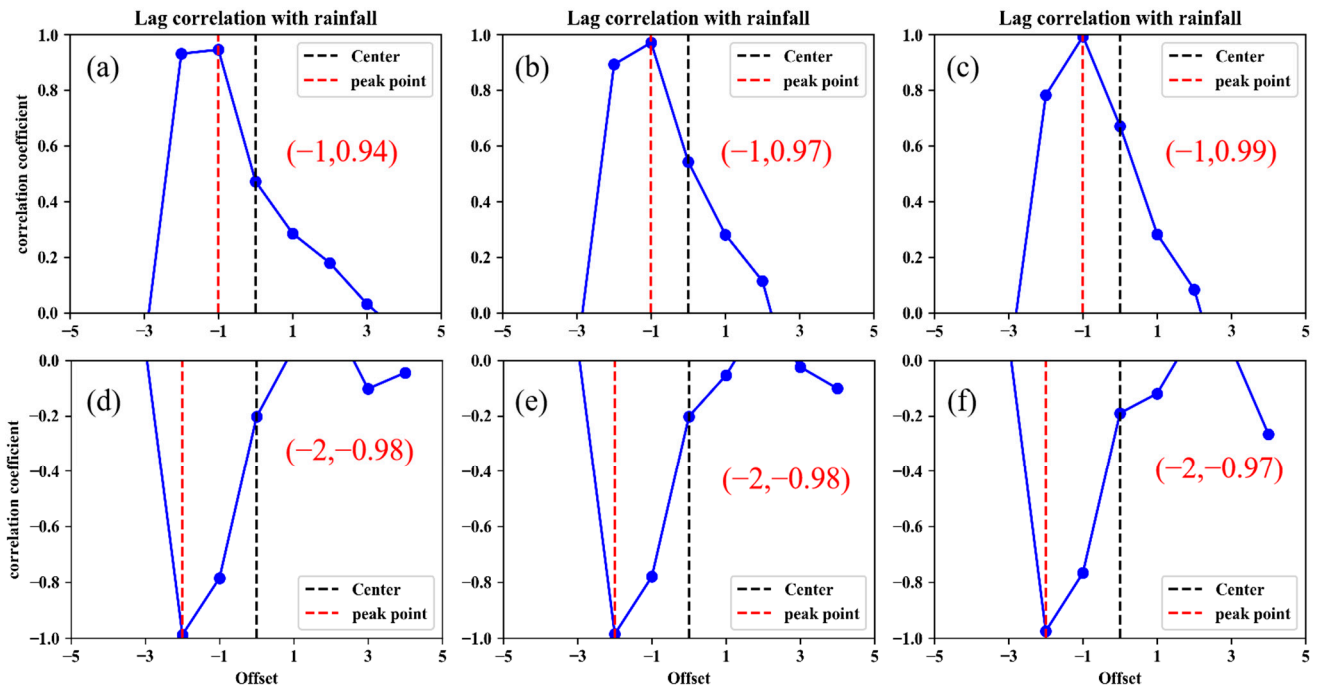
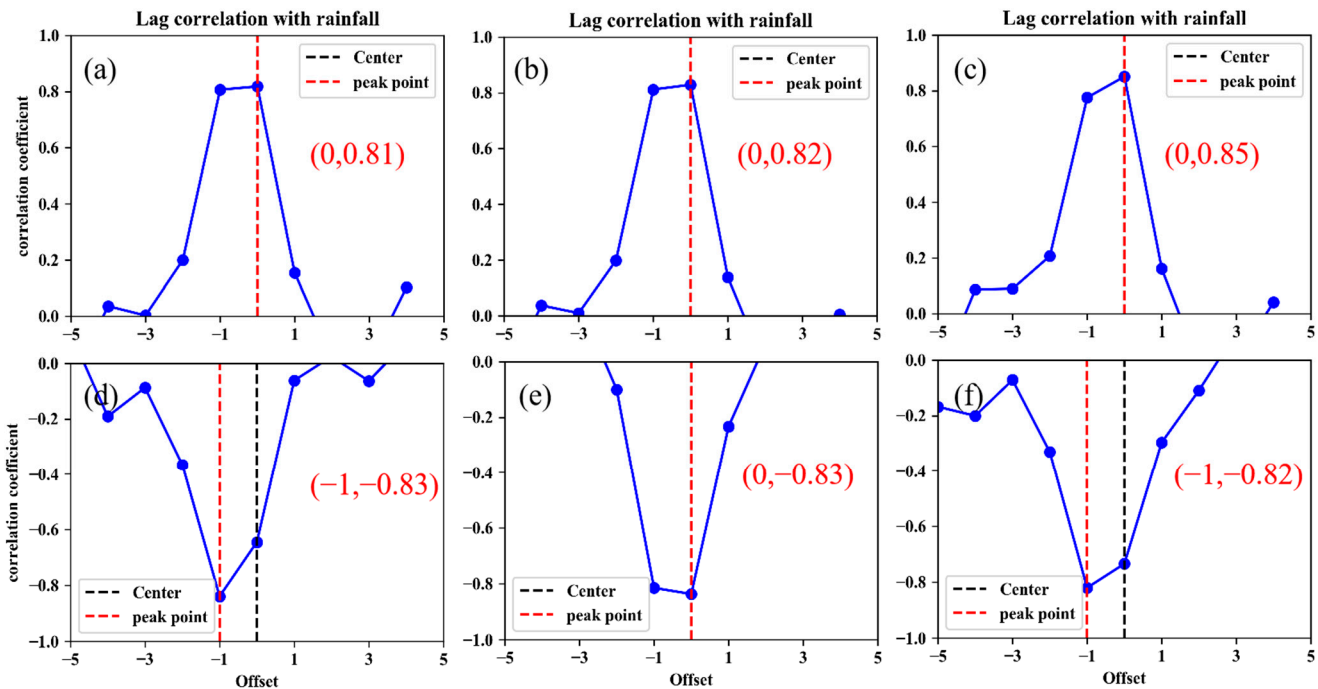


Figure 18. GNSS warning parameters and multi-source monitoring data changes during the second instability periods: (a) NN06; (b) NN07; (c) NN08.



**Figure 19.** Lag correlation between displacement rate and rainfall in the first failure. (a)–(c) are lag correlation between horizontal displacement velocity and rainfall, (d)–(f) are lag correlation between vertical displacement velocity and rainfall.



**Figure 20.** Lag correlation between displacement rate and rainfall in the second failure. (a)–(c) are lag correlation between horizontal displacement velocity and rainfall, (d)–(f) are lag correlation between vertical displacement velocity and rainfall.

### 6.2. GNSS Tangent Angle Characteristics in Expansive Soil Landslide Early Warning

By summarizing two GNSS tangent angle real-time curves, it was found that the GNSS tangent angle had oscillating characteristics if the slope was in the stable deformation phase. The subtle deformation was drowned by the GNSS measurement noise at this stage. When landslide mass entered the accelerated deformation stage, the GNSS tangent angle

took on a monotonous upward trend and gradually approached  $80^\circ$ . If the GNSS tangent angle exceeded  $80^\circ$ , the slope was able to enter the accelerated deformation period. This is because when the slope entered the accelerated phase, especially for sudden landslides, the magnitude of the displacement incremented gradually beyond the GNSS measurement noise. The displacement rapidly increased during the monitoring period, and the tangent angle lost its oscillation characteristics.

When most slopes were about to lose stability, the tangent angle would approach  $90^\circ$ . The Ningming Basin has medium-expansive soil, which will be rapidly deformed in the case of heavy rainfall, and this deformation can accelerate to slope failure within a few hours. Therefore, the alarm threshold of the GNSS tangent angle was reduced to  $85^\circ$ , which reserves enough time for deploying landslide prevention measures. In addition, the tangent angle must be combined with another parameter for warning at the same time. It is also common in the case where the tangent angle value exceeds  $85^\circ$  due to a temporary acceleration of slope deformation, while the displacement rate does not exceed the alarm limit.

### 6.3. Assistance of GNSS Monitoring to Early Warning of Expansive Soil Slope

After the slope failure, a site survey of this geological hazard was conducted on 19 February 2022, and the slip direction of the monitoring stations was identical to the GNSS monitoring results. The cumulative displacements of NN06, NN07, and NN08 were 537.61, 430.92, and 284.90 mm, respectively. Most deformed parts were located on the slope shoulders, as the terrain of this area is relatively gentle. The soil showed fragmentation and slight settlement but without overall slide. The detailed fractures near the monitoring stations after the first instability are shown in Figure 21. The yellow areas in Figure 21a–c are fractures distributed by shallow instability, and the fissures of fracture closure were not obvious. The average widths near NN06, NN07, and NN08 were 1.3, 0.9, and 0.8 cm, respectively.

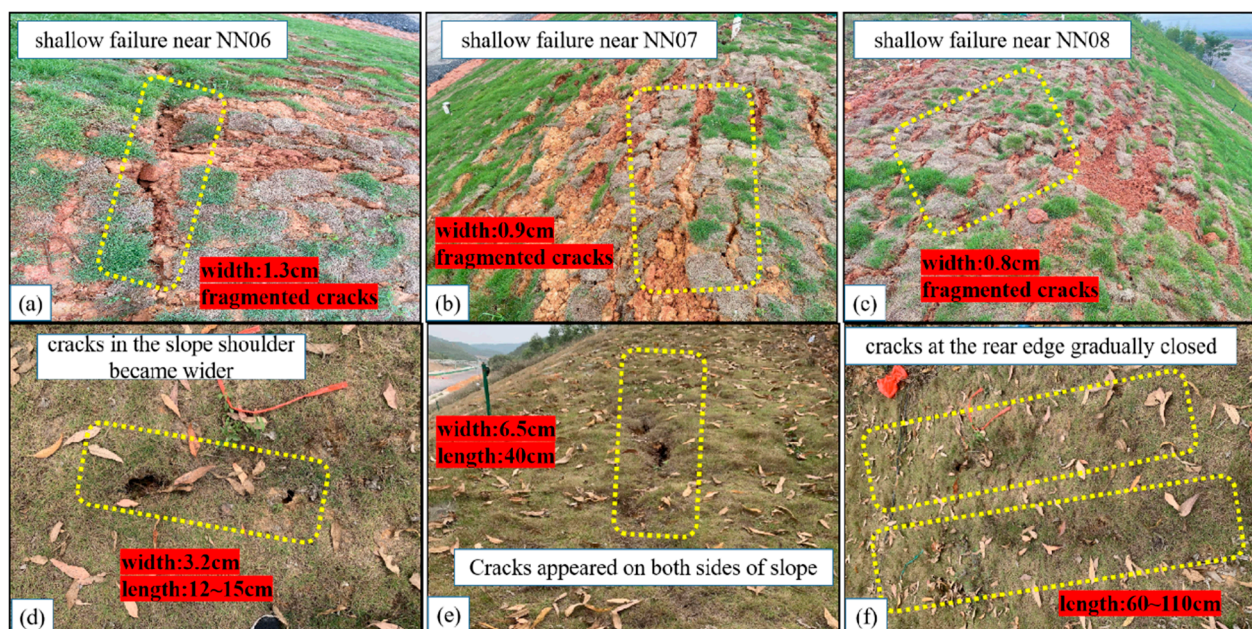


**Figure 21.** Cracks change after the two failure of slope: (a–c) Cracks change after the first failure; (d–f) cracks change after the second failure.

After the second instability, the depth of the fissures on both sides of the slope and its shoulder were increased (see Figure 21d,e), and the average width and length were 3.2 and 6.5 cm and 13 and 40 cm. Many cracks at the trailing edge of the slope are gradually closed, which are shown in Figure 21f, indicating that the significant deformation of GNSS

not only has a time–response relationship with multi-source data but also has a consistent spatial-matching feature with the development of cracks in the slope. Most expansive soil slopes in the Ningming Basin were gently expansive soil slopes. The characteristics of fissures and shallow layers were the main factors for the instability risk of gentle slopes. Several pieces of GNSS monitoring equipment were scientifically deployed in the area where the main cracks developed, as they could monitor the shallow deformation of the slope in real time, providing a data basis for early warning. In addition, with the increasing demand for modern disaster monitoring, low-cost GNSS acquisition of real-time high-accuracy shallow deformation and main slip direction will be conducive to large-scale monitoring and warning of expansive soil disasters. The early-warning model based only on one single GNSS displacement and its derived parameters could preliminarily judge the deformation stage of the landslide mass and successfully forewarned slope failure twice. Both instantaneity and efficiency are considered in this model, which can provide a certain reference for other fields of expansive soil hazards.

## 7. Conclusions

1. The stability of expansive soil landslides can be directly reflected by shallow displacement. To dynamically conduct early warning for Ningming's expansive soil slopes, a monitoring demonstration area with GNSS and multi-source sensors was constructed. A real-time early-warning model based on the GNSS shallow displacement rate and improved tangent angle was proposed based on the measured displacement of self-developed GNSS sensors. The warning thresholds for different deformation stages were preliminarily defined and provided the implementation process of the GNSS real-time warning system for expansive soil landslides. A three-level warning system (first level, second level, and alarm level) was established. Complex slope mechanics do not require modeling and calculation, and the real-time early warning of expansive soil instability can be realized;
2. The Ningming expansive soil slope instability was successfully warned by the proposed method twice. A time response between the GNSS warning parameters and external multi-source monitoring data was found, and the development of fissures around the monitoring station has matching spatial variation characteristics with GNSS displacement. The feasibility of expansive soil failure warning relying on single GNSS technology can be verified. Compared to traditional warning methods, it has advantages in cost and timeliness, and the stability of different detailed positions of slopes can be simultaneously analyzed, which is beneficial for modern universal disaster warning needs. To some extent, it has reference value for the early warning of expansive soil landslides in Ningming and other regions.

**Author Contributions:** Conceptualization, G.H.; methodology, Z.C.; validation, Y.Z.; formal analysis, G.H.; investigation, Z.C.; resources, Z.C.; writing—review and editing, W.X.; visualization, L.W.; supervision, L.W.; All authors have read and agreed to the published version of the manuscript.

**Funding:** This research was funded by the National Key Research and Development Program of China (Grant No. 2019YFC1509802).

**Acknowledgments:** The multi-source data in this study were provided by Wuhan University. Xu Yongfu of Shanghai Jiaotong University and Guangxi Jiaotong Technology Group provided guidance and assistance. We are very grateful for the above support.

**Conflicts of Interest:** The authors declare no conflict of interest.

## References

1. Mohammad, S.K.; Sahadat, H.; Asif, A.; Mohammad, F. Investigation of a shallow slope failure on expansive clay in Texas. *Eng. Geol.* **2017**, *219*, 118–129. [[CrossRef](#)]
2. Lei, W.K.; Dong, H.Y.; Chen, P.; Lv, H.B.; Fan, L.Y.; Mei, G.X. Study on Runoff and Infiltration for Expansive Soil Slopes in Simulated Rainfall. *Water* **2020**, *12*, 222. [[CrossRef](#)]

3. Zhan, T.L.; Ng, C.W.; Fredlund, D.G. Field study of rainfall infiltration into a grassed unsaturated expansive soil slope. *Can. Geotech. J.* **2007**, *44*, 392–408. [[CrossRef](#)]
4. Zhang, S.C.; Si, J.Z.; Niu, Y.F.; Zhu, W.; Qian, F.; Hu, X.Q.; Zhang, C.B.; An, P.; Ren, Z.P.; Li, Z.H. Surface Deformation of Expansive Soil at Ankang Airport, China, Revealed by InSAR Observations. *Remote Sens.* **2022**, *14*, 2217. [[CrossRef](#)]
5. Shi, B.; Jiang, H.T.; Liu, Z.B.; Fang, H.Y. Engineering geological characteristics of expansive soils in China. *Eng. Geol.* **2002**, *67*, 63–71. [[CrossRef](#)]
6. Rubayet, B.M.; Carol, J.F.; Robert, V.R.; Nazla, B.; Chad, L.H. Property Risk Assessment for Expansive soils in Louisiana. *Front. Built Environ.* **2021**, *7*, 754761. [[CrossRef](#)]
7. Zhan, L.; Chen, R.; Ng, C.W.W. Wetting-induced softening behavior of an unsaturated expansive clay. *Landslides* **2014**, *11*, 1051–1061. [[CrossRef](#)]
8. Pathak, Y.P.; Alfaro, M.C. Wetting-drying behavior of geogrid reinforced clay under working load conditions. *Geosynth. Int.* **2010**, *17*, 144–156. [[CrossRef](#)]
9. Rodriguez, J.; Deane, E.; Hendry, M.T.; Macciotta, R. Practical evaluation of single-frequency dGNSS for monitoring slow-moving landslides. *Landslides* **2021**, *18*, 3671–3684. [[CrossRef](#)]
10. Panagiotis, A.; Athanassios, G.; Sotirios, V.; Vasiliou, T.; Nikolaos, S.; Basil, P. Anthropogenically induced subsidence in Thessaly, central Greece: New evidence from GNSS data. *Nat. Hazards* **2020**, *102*, 179–200. [[CrossRef](#)]
11. Zhang, Q.; Bai, Z.W.; Huang, G.W.; Du, Y.; Wang, D. Review of GNSS Landslide Monitoring and Early Warning. *Acta Geod. Et Cartogr. Sinica* **2022**, *51*, 1985–2000. (In Chinese)
12. Li, Z.; Zang, J.; Fan, S.; Wen, Y.; Xu, C.; Yang, F.; Peng, X.; Zhao, L.; Zhou, X. Real-Time Source Modeling of the 2022 Mw 6.6 Menyuan, China Earthquake with High-Rate GNSS Observations. *Remote Sens.* **2022**, *14*, 5378. [[CrossRef](#)]
13. Struhár, J.; Rapant, P.; Kačmařík, M.; Hlaváčová, I.; Lazecký, M. Monitoring Non-Linear Ground Motion above Underground Gas Storage Using GNSS and PSInSAR Based on Sentinel-1 Data. *Remote Sens.* **2022**, *14*, 4898. [[CrossRef](#)]
14. Orellana, F.; Hormazábal, J.; Montalva, G.; Moreno, M. Measuring Coastal Subsidence after Recent Earthquakes in Chile Central Using SAR Interferometry and GNSS Data. *Remote Sens.* **2022**, *14*, 1611. [[CrossRef](#)]
15. Dai, W.; Dai, Y.; Xie, J. Back-Analysis of Slope GNSS Displacements Using Geographically Weighted Regression and Least Squares Algorithms. *Remote Sens.* **2023**, *15*, 759. [[CrossRef](#)]
16. Šegina, E.; Peternel, T.; Urbančič, T.; Realini, E.; Zupan, M.; Jež, J.; Caldera, S.; Gatti, A.; Tagliaferro, G.; Consoli, A.; et al. Monitoring Surface Displacement of a Deep-Seated Landslide by a Low-Cost and near Real-Time GNSS System. *Remote Sens.* **2020**, *12*, 3375. [[CrossRef](#)]
17. Orellana, F.; Moreno, M.; Yáñez, G. High-Resolution Deformation Monitoring from DInSAR: Implications for Geohazards and Ground Stability in the Metropolitan Area of Santiago, Chile. *Remote Sens.* **2022**, *14*, 6115. [[CrossRef](#)]
18. Kang, Y.; Zhao, C.; Zhang, Q.; Lu, Z.; Li, B. Application of InSAR Techniques to an Analysis of the Guanling Landslide. *Remote Sens.* **2017**, *9*, 1046. [[CrossRef](#)]
19. Corsa, B.; Barba-Sevilla, M.; Tiampo, K.; Meertens, C. Integration of DInSAR Time Series and GNSS Data for Continuous Volcanic Deformation Monitoring and Eruption Early Warning Applications. *Remote Sens.* **2022**, *14*, 784. [[CrossRef](#)]
20. Han, J.; Yang, H.; Liu, Y.; Lu, Z.; Zeng, K.; Jiao, R. A Deep Learning Application for Deformation Prediction from Ground-Based InSAR. *Remote Sens.* **2022**, *14*, 5067. [[CrossRef](#)]
21. Yang, R.; Xiao, P.W.; Qi, S.C. Analysis of slope stability in unsaturated expansive soil: A case study. *Front. Earth Sci.* **2019**, *7*, 292. [[CrossRef](#)]
22. Dai, Z.J.; Guo, J.H.; Luo, H.M.; Li, J.; Chen, S.X. Strength Characteristics and Slope Stability Analysis of Expansive Soil with Filled Fissures. *Appl. Sci.* **2020**, *10*, 4616. [[CrossRef](#)]
23. Chen, L.; Zhang, P.; Lu, S. Analysis of Typical Expansive Soil Slope Project. In Proceedings of the 2nd International Conference GEDMAR08, Nanjing, China, 30 May–2 June 2008; pp. 487–491.
24. Xu, Q.; Tang, M.G.; Huang, R.Q. *Large-Scale Landslide Monitoring, Early Warning and Emergency Response*; Science Press: Beijing, China, 2015; pp. 20–35. ISBN 978-7-03-043369-5.
25. Kim, Y.M.; Harianto, R.; Margarit, M.N.; Alfrendo, S. Assessment of critical rainfall scenarios for slope stability analyses based on historical rainfall records in Singapore. *Environ. Earth Sci.* **2022**, *81*, 39. [[CrossRef](#)]
26. Zhu, X.X.; Zhang, L.; Yang, S.W. Characteristics of rainfall-induced loess landslides and their threshold rainfall in Lanzhou. *Chin. J. Geol. Hazard Control.* **2019**, *4*, 4. (In Chinese)
27. Zhang, J.J.; Gong, B.W.; Hu, B.; Zhou, X.W.; Wang, J. Study of evolution law of fissures of expansive clay under wetting and drying cycles. *Rock Soil Mech.* **2011**, *32*, 2729–2734. (In Chinese)
28. Ye, W.M.; Kong, L.W.; Hu, R.L. New prevention and treatment techniques and their applications to landslides and engineering slopes of expansive soils. *Chin. J. Geotech. Eng.* **2022**, *44*, 1295–1309.
29. Xu, Q.; Peng, D.L.; He, C.Y.; Qi, X.; Zhao, K.Y.; Xiu, D.H. Theory and method of monitoring and early warning for sudden loess landslide—A case study on the Heifangtai terrace. *Eng. Geol.* **2020**, *28*, 111–121. [[CrossRef](#)]
30. Yang, G.L.; Chen, Z.; Zhang, H.R. Collapse mechanism of gentle expansive soil slope in drying and wetting cycles. *J. Cent. South Univ. Sci. Technol.* **2022**, *53*, 95–103.
31. Huang, G.W.; Chen, Z.; Xu, Y.F. GNSS Real-time Monitoring Technology of Expansive Soil Slope. *Acta Geod. Et Cartogr. Sinica.* **2023**, *4*, 5. (In Chinese)

32. Yang, H.P.; Qu, Y.X.; Zheng, J.L. New development in studies on Ningming expansive soils. *Chin. J. Geotech. Eng.* **2005**, *9*, 981–987. (In Chinese)
33. Chen, Z.H. On basic theories of unsaturated soils and special soils. *Chin. J. Geotech. Eng.* **2014**, *36*, 201–272. (In Chinese)
34. Wang, X.Q.; Xu, C.; Wang, S.J.; Li, X. Study on overburden pressure effect of expansive soil water characteristic curve. *Chin. J. Rock Mech. Eng.* **2020**, *39*, 56–58. (In Chinese) [[CrossRef](#)]
35. Farzaneh, G.; Jacopo, D.R.; Alessandro, G.; Caterina, D.M. Swelling and swelling pressure of a clayey soil: Experimental data, model simulations and effects on slope stability. *Eng. Geol.* **2022**, *297*, 106512. [[CrossRef](#)]
36. Pei, P.; Zhao, Y.L.; Ni, P.P.; Mei, G.X. A protective measure for expansive soil slopes based on moisture content control. *Eng. Geol.* **2020**, *269*, 105527. [[CrossRef](#)]

**Disclaimer/Publisher’s Note:** The statements, opinions and data contained in all publications are solely those of the individual author(s) and contributor(s) and not of MDPI and/or the editor(s). MDPI and/or the editor(s) disclaim responsibility for any injury to people or property resulting from any ideas, methods, instructions or products referred to in the content.